



**HAL**  
open science

# Drop rise and interfacial coalescence initiation in Bingham materials

Lucas H.P. Deoclecio, Edson Soares, Stéphane Popinet

► **To cite this version:**

Lucas H.P. Deoclecio, Edson Soares, Stéphane Popinet. Drop rise and interfacial coalescence initiation in Bingham materials. *Journal of Non-Newtonian Fluid Mechanics*, 2023, 319, pp.105075. 10.1016/j.jnnfm.2023.105075 . hal-04142183

**HAL Id: hal-04142183**

**<https://hal.science/hal-04142183>**

Submitted on 26 Jun 2023

**HAL** is a multi-disciplinary open access archive for the deposit and dissemination of scientific research documents, whether they are published or not. The documents may come from teaching and research institutions in France or abroad, or from public or private research centers.

L'archive ouverte pluridisciplinaire **HAL**, est destinée au dépôt et à la diffusion de documents scientifiques de niveau recherche, publiés ou non, émanant des établissements d'enseignement et de recherche français ou étrangers, des laboratoires publics ou privés.

# Drop rise and interfacial coalescence initiation in Bingham materials

Lucas H. P. Deoclecio<sup>a</sup>, Edson J. Soares<sup>a</sup>, Stéphane Popinet<sup>b</sup>

<sup>a</sup>*LABREO, Department of Mechanical Engineering, Universidade Federal do Espírito Santo, Avenida Fernando Ferrari, 514, Goiabeiras, 29075-910, ES, Brazil*

<sup>b</sup>*Sorbonne Université and CNRS, Institut Jean Le Rond d'Alembert UMR 7190, F-75005 Paris, France*

---

## Abstract

Drop coalescence in viscoplastic materials is present in various industrial applications and the environment. The plasticity of the surrounding material affects drop rise, collision, and film drainage dynamics, and knowledge about these is essential for designing and operating industrial mixer and separator units. Despite its importance, the coalescence of drops in yield stress materials is not entirely understood. In this work, we investigate the effects of the surrounding material plasticity on the rise and interfacial coalescence initiation of Newtonian drops using direct numerical simulations. Plastic effects contribute to the formation of smaller and spherical films, which facilitate the film drainage process on the one hand, but also to an increase in the resistance of the film to flow, which makes the drainage process more difficult on the other hand. The fluids' interfaces are less deformable for high surface tension regimes, and the flow resistance effects become more significant than the film shape change effects. As a result, the drainage time tends to

---

*Email addresses:* `edson.soares@ufes.br` (Edson J. Soares), +55 27 33579500 5028 (Edson J. Soares)

increase with the level of plasticity. For low surface tension regimes, the fluid interface is more deformable, and film drainage time tends to decrease with an increase in the level of plasticity.

*Keywords:* Drop coalescence, Drop rise, Film drainage, Viscoplastic materials, Yield stress.

---

## 1. Introduction

Drop coalescence in viscous liquids is a fundamental problem in fluid mechanics, and it is relevant in the environment and many industrial mixing and separation processes. In many cases, the surrounding fluid is a yield stress material, such as in processing food, cosmetics, medicines, waste, slurries, inks, and crude oil, to name a few (Dubash and Frigaard, 2004, 2007; Goel and Ramachandran, 2017; Tripathi et al., 2015; de Souza Mendes, 2011). Depending on the application, phase separations (rise and coalescence) may be desirable or undesirable. Drop rise and coalescence are desirable in treating crude oil and liquid–liquid extraction to recover the added value component and discard treated residues. On the other hand, bubbles and drops entrapped are desirable in food processing, such as chocolate, ketchup, and mayonnaise, to improve their taste. Their entrapment is also desirable in the processing of cosmetic lotions and medicine. This work uses the term drop as the general case regardless of the density and viscosity ratios. In contrast, the term bubble is reserved for the case where the internal phase is a gas (small density and viscosity ratios).

Understanding the basic mechanisms of coalescence is fundamental to the scale-up of industrial processes (Charin et al., 2019). For instance, the con-

ception of coalescence models based on single-drop systems may be used as an input for predicting particle size distribution in industrial oil/water separators using the Population Balance Equation approach (Deoclecio et al., 2020). Coalescence may take place between two drops, or between a drop and a fluid-fluid interface. The coalescence process is similar in both, and in some cases theoretical solutions may even become the same via the equivalent radius principle (Chesters, 1991; Oldenziel et al., 2012). It may be divided into four sequential steps: collision, film drainage, film rupture, and merging (Goel and Ramachandran, 2017; Liao and Lucas, 2010; Mohamed-Kassim and Longmire, 2003; Chesters, 1991). The collision step results from the action of external forces (*e.g.*, hydrodynamics, and gravity). For interfacial coalescence, the collision is a function of the drop rise dynamics, which depends on the density and rheological properties of the phases, drop size, surface tension, and interface mobility (Balla et al., 2020; Charin et al., 2019; Chhabra, 2006; Clift et al., 2005; Zenit and Magnaudet, 2008). The drop collision is a highly dynamic process, and it sets the initial condition for the film drainage step, thus playing a crucial role in the coalescence phenomenon (Zawala et al., 2020; Zawala and Malysa, 2011). During the collision step, a thin film of the surrounding materials is trapped between the drop and the interface (or between two drops). This film must be drained out, so the fluid interfaces may come nearby for coalescence. The drainage process usually is the coalescence controlling rate step (Chesters, 1991; Kamp et al., 2017; Henschke et al., 2002). Film rupture happens when the film thickness is small enough that non-hydrodynamic forces (*e.g.* van der Waals) destabilize and break the film. After film rupture, the last step, merging the fluid bodies

driven by surface tension, takes place.

During the drainage process, the external squeezing forces give rise to a radial pressure gradient within the draining film that deforms the fluid interfaces and acts against viscous forces to drain out the surrounding phase (Chan et al., 2011). The viscosity ratio between the phases ( $\mu_r = \mu_d/\mu_s \ll 1$ , where  $\mu_d$  is the viscosity of the drop and  $\mu_s$  is the viscosity of the surrounding) controls (for contaminant-free systems) the fluid interface mobility. Experimental results of Aarts and Lekkerkerker (2008) of gas bubbles and liquid drops coalescence with an interface indicate that the film rupture tends to occur at the film center for the former and on one of the film sides for the latter. For mobile interface systems (low viscosity ratio), as in the case of bubbles, the pressure gradient in the film is weak and the film tends to have a spherical shape (minimum thickness at the film center and increasing monotonically with film radius). For immobile or partially mobile interfaces (high viscosity ratio), as in the case of liquid drops, the pressure gradient in the film is more substantial and the film tends to form a dimple, where the minimum film thickness is at the film periphery (Chi and Leal, 1989; Oldenzel et al., 2012; Liu et al., 2019). The surface tension coefficient and drop collision dynamics also influence the film shape. Kočárková et al. (2013) experimentally investigated the effect of the Bond number (the ratio of buoyancy to surface tension forces) on drop coalescence. The authors found that an increase in the Bond number tends to increase the film surface area and reduce the average pressure in the film. This increased the drainage time. Zawala and Malysa (2011) assessed the effect of the drop impact velocity on the film length and drainage time. An increase in the impact velocity led to

more significant drop width and film length increase due to the conversion of kinetic to surface tension energy. This, consequently, led to an increase in the drainage time. Also, experimental results of (Doublier, 1991) show that collisions of tiny bubbles with small impact velocities increase the probability of coalescence to happen.

It is common practice to hinder or facilitate coalescence by adding or removing surfactants on the interface, respectively. Besides changing the boundary conditions for the flow in the film by rendering the interfaces immobile, the contamination of the interfaces also affects the resultant short-range non-hydrodynamic forces that govern the film rupture. Surfactants adsorbed on the interface generally stabilize the film by strengthening the non-hydrodynamic repulsive forces (Zawala et al., 2020; Goel and Ramachandran, 2017). Thus, for Newtonian films, which most studies focus on, interfacial coalescence may be inhibited by adding a surfactant to the interface to prevent the film's rupture. However, if the surrounding material presents a viscoplastic behavior, coalescence may be prevented before the short-range non-hydrodynamic forces come to play. The first concept of viscoplastic fluid was proposed by Bingham (1922) who states that viscoplastic materials behave like a solid when the applied stress is below the limit called yield stress, and behave like a fluid when the applied stress is higher than the yield stress. Therefore, drops and bubbles may become entrapped if the buoyancy force is insufficient to overcome the surrounding phase yield stress (Dubash and Frigaard, 2007; Deoclecio et al., 2021), preventing the collision step from happening. Coalescence can also be inhibited in the case of mobile drops if the stress in the draining film becomes less than the surrounding mate-

rial yield stress. Even if coalescence is not prevented, the yield stress alters the collision and film drainage dynamics, which influences the coalescence rate (Hartland and Jeelani, 1986, 1987; Goel and Ramachandran, 2017). Thus, understanding the drainage dynamics of viscoplastic films may aid in selecting appropriate strategies to stabilize or destabilize a dispersed system; for instance, avoiding a waste of emulsifiers and demulsifiers (Tchoukov et al., 2014). Hartland and Jeelani (1986, 1987) obtained expressions for the freezing thickness (when the drainage process come to a halt due to the yield stress) of dimpled and planar films of Bingham materials, respectively. Nevertheless, these studies suffer from ad-hoc assumptions about the drop impact condition and the film shape. Goel and Ramachandran (2017) argued these ad-hoc assumptions lead to incorrect predictions of the level of plasticity required to inhibit coalescence. The authors used scaling analysis and lubrication theory to model the drainage dynamics of films of Bingham materials. According to the authors' results, the yield stress cannot arrest spherical films. Only dimpled films can be frozen before a thickness at which intermolecular forces assist the drainage process. Sanjay et al. (2021) numerically studied the bursting of bubbles at a fluid-fluid interface in Bingham materials. The authors model the last step of the coalescence process, the merging of the fluid bodies after film rupture. The bubbles were spherical and the dynamics of bubble collision and film drainage were not assessed. They showed that the free surface converges to a non-flat final equilibrium shape which depends on the balance between the surrounding material yield stress and surface tension. They also showed that the yield stress damps the capillary waves and slows down the flow during the merging step.

Studies on the drop coalescence process in viscoplastic materials, especially the collision and film drainage steps, are still rare in the literature. Consequently, the effects of the yield stress on drop collision and film drainage dynamics are not entirely understood. By using time-dependent numerical simulations, we attempt to deepen the understanding of the role played by the yield stress of the surrounding fluid on the coalescence process, taking into account the drop rise dynamics before the collision. We focus our study on the collision and the initial stage of film drainage, which may be seen as an indicator of the coalescence rate. The Bingham model is used to mimic the yield stress characteristics of the viscoplastic material. The rest of the paper is organized as follows. Section 2 describes the problem formulation and presents the computational domain, boundary conditions, governing equations, and dimensionless numbers. Next, Sec. 3 shows validation tests to verify the solver accuracy and grid dependency. Then, Sec. 4 presents the results and discussion. Finally, Sec. 5 summarizes the main conclusions.

## 2. Problem Formulation

We investigate the rise and interfacial coalescence of Newtonian drops in Bingham materials using direct numerical simulations in an axisymmetric geometry. In this section, we first present the computational domain along with the boundary and initial conditions. Then, we give the governing equations and the important dimensionless parameters.

### 2.1. Computational domain

Fig. 1(a) shows a representative diagram of the computational domain. The simulations are performed in a square domain of height  $H = 25 D$ , where



$D$  is the diameter of the initially spherical drop. Axisymmetric simulations are performed in a cylindrical coordinate system  $(r, z)$  where the axis of symmetry lies along the  $z$ -axis (the right boundary). The origin of the coordinate system lies at the crossing of the interface rest position with the axis of symmetry, as shown in Fig. 1(a). The interface depth,  $z_i = 5D$ , is sufficient to avoid boundary effects. The rising distance,  $z_r$ , corresponds to the distance between the initial drop position,  $z_o$ , and the interface rest position,  $z = 0$ .  $z_r$  varies as a function of the distance needed for the drop to reach its terminal velocity before interacting with the interface to reduce the processing time. The surrounding viscoplastic fluid (represented as Fluid 1) is modeled using the Bingham constitutive equations while the drop and the interface (represented as Fluid 2) are composed of the same Newtonian fluid. Gravity acts in the negative  $z$ -direction. Initially, both fluids are at rest. We apply free-slip boundary conditions without mass penetration for the velocity field at the bottom, left, and top boundaries. In addition, the Neumann boundary condition for the pressure field is applied at these boundaries. The size of the computational domain  $H$  and top layer interface depth  $z_i$  are sufficiently large to avoid boundary effects. Doubling  $H$  and reducing  $z_i$  by half changed the drop terminal velocity and computational drainage time (defined in the sequence) in less than 1% and 0.15%, respectively.

Fig. 1(b) presents a scheme of a drop impacting an interface and subsequently trapping and draining a film of the surrounding fluid (Fluid 1). To study the flow in the film, we define a new non-orthogonal coordinate system  $(s, h)$  with a moving origin located at the drop's "tip." The coordinate  $s$  follows the drop surface, and the coordinate  $h$  is in the direction of the

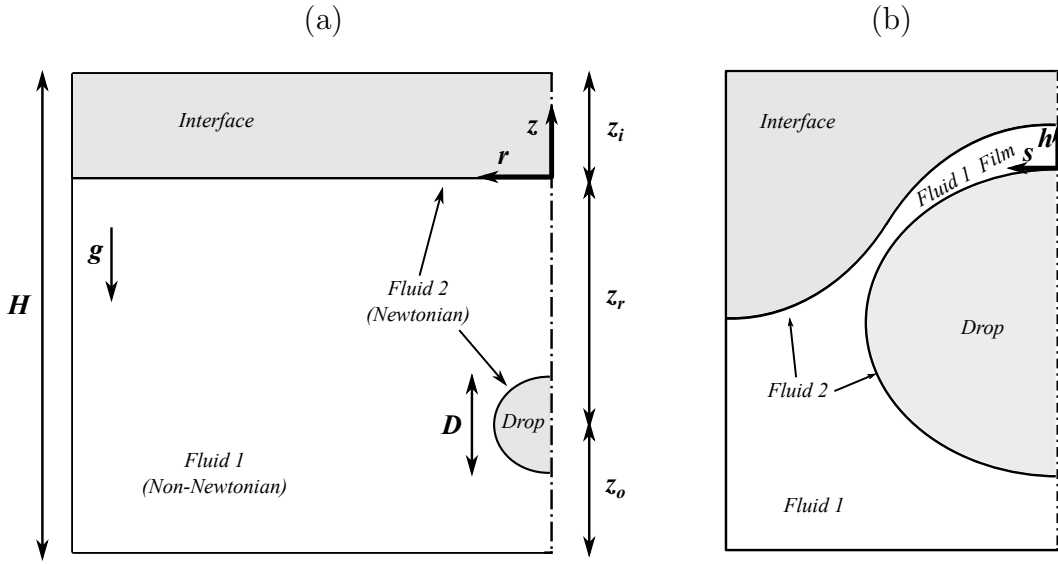


Figure 1: A representative diagram of the computational domain. The numerical simulations are performed in (a) square domain of side length  $H = 25D$ , where  $D$  is the diameter of the drop. The axisymmetric simulations are performed in a cylindrical coordinate system  $(r, z)$  where  $r$  and  $z$  are the radial and axial coordinates, respectively. Gravity acts in the negative  $z$ -direction. The surrounding is a viscoplastic fluid (Fluid 1), and the drop and the interface are composed of the same Newtonian fluid (Fluid 2). (b) A scheme representing the drop impact on the top layer interface and trapping of a film of the surrounding viscoplastic material. The film shape is studied in a non-orthogonal coordinate system  $(s, h)$ , where  $s$  follows the drop surface and  $h$  points to the direction of the closest point on the interface from the drop surface.

closest point on the upper fluid surface (the top layer) from the point  $(s, 0)$  on the lower fluid surface (the drop). Hence, the  $h$ -direction is generally not normal to the drop surface. Due to the computational cost of performing numerical simulations up to the film rupture thickness (in the range of the non-hydrodynamic forces), we infer the effect of the yield stress on the coalescence time based on the computational drainage time,  $\Delta t$ , defined as the time elapsed between the minimum distance between the drop and the top layer interface thins from  $h_{min} = 0.1 D$  to  $0.01 D$  (note that the film rupture thickness is generally less than  $0.01 D$ ).

## 2.2. Governing equations

In the present simulations, the fluids are considered incompressible, and the governing mass and momentum conservation equations are as follows

$$\nabla \cdot \mathbf{u} = 0, \quad (1)$$

$$\rho \left[ \frac{\partial \mathbf{u}}{\partial t} + \mathbf{u} \cdot \nabla \mathbf{u} \right] = -\nabla p + \nabla \cdot [\mu (\nabla \mathbf{u} + \nabla \mathbf{u}^T)] + \mathbf{f}_\sigma - \rho \mathbf{g}. \quad (2)$$

Here,  $\mathbf{u}$  ( $u_r, u_z$ ) is the velocity field, where  $u_r$  and  $u_z$  are the velocity components in the radial ( $r$ ) and axial ( $z$ ) directions, respectively;  $p$  is the pressure field;  $\mathbf{g} = g\mathbf{e}_z$  where  $g$  is the acceleration due to gravity and  $\mathbf{e}_z$  is the unit vector in the negative  $z$ -direction;  $\rho$  is the density field;  $\mu$  is the viscosity field;  $t$  is time;  $\mathbf{f}_\sigma$  is the local density of capillary force per unit volume and is equal to  $\mathbf{f}_\sigma = \sigma \kappa \mathbf{n} \delta_s$ , where  $\sigma$  is the surface tension coefficient,  $\kappa$  is the

mean curvature of the interface,  $\delta_s$  is the Dirac delta function, which is zero everywhere except at the interface, and  $\mathbf{n}$  is the unit normal to the interface.

The bulk fluid is viscoplastic (Fluid 1), while the drop and the interface are Newtonian fluids (Fluid 2). The respective densities of the two liquids,  $\rho_1$  and  $\rho_2$ , are constants. The viscosity  $\mu_2$  of the Newtonian phase is constant while the viscosity of the bulk viscoplastic phase,  $\mu_1$ , is modeled using a regularized version of the Bingham constitutive law given by (Bingham, 1922; Frigaard and Nouar, 2005; Allouche et al., 2000; Balmforth et al., 2014)

$$\mu_1 = \mu_p + \frac{\tau_y}{\|\dot{\gamma}\| + \epsilon}. \quad (3)$$

Here,  $\mu_p$  is the plastic viscosity of the Bingham model;  $\tau_y$  is the yield stress;  $\|\dot{\gamma}\| = \sqrt{(1/2)\dot{\gamma} : \dot{\gamma}}$  is the Frobenius norm of the strain rate tensor  $\dot{\gamma}$ . The regularization parameter  $\epsilon$  is calculated as

$$\epsilon = \frac{\tau_y}{N\mu_c}, \quad (4)$$

where  $\mu_c = \mu_p + \tau_y/\dot{\gamma}_c$  is the characteristic viscosity based on the characteristic strain rate  $\dot{\gamma}_c$  (defined later) and  $N$  is the dimensionless regularization parameter whose value is large. We conduct a convergence test to optimize the value of  $N$ , presented in Sec. 3. The yielded (unyielded) regions are separated based on the von Mises criterion given as  $\|\boldsymbol{\tau}\| > \tau_y$  ( $\|\boldsymbol{\tau}\| \leq \tau_y$ ), where  $\|\boldsymbol{\tau}\|$  is the magnitude of the deviatoric stress tensor.

The advection equation for the volume fraction field  $\alpha$  is solved to track the interfaces separating the fluids,

$$\frac{\partial \alpha}{\partial t} + \mathbf{u} \cdot \nabla \alpha = \mathbf{0}. \quad (5)$$

$\alpha$  is taken as 0 and 1 for Fluid 1 and Fluid 2, respectively. The density  $\rho$  and viscosity  $\mu$  fields are then calculated based on volume fractions in each grid cell as

$$\rho = \rho_1(1 - \alpha) + \rho_2(\alpha) \quad (6)$$

$$\mu = \frac{1}{\frac{1-\alpha}{\mu_1} + \frac{\alpha}{\mu_2}}. \quad (7)$$

### 2.3. Non-dimensional parameters

The following scalings are used to non-dimensionalize the governing equations and boundary conditions:

$$\begin{aligned} (\bar{r}, \bar{z}) &= (r/D, z/D), (\bar{s}, \bar{h}) = (s/D, h/D), \bar{\mathbf{u}} = \mathbf{u}/U, \bar{t} = t/t_c, \bar{P} = P/\rho_1 U^2, \\ \bar{\mu} &= \mu/\mu_c, \bar{\rho} = \rho/\rho_1, \bar{\dot{\gamma}} = \dot{\gamma}/\dot{\gamma}_c \end{aligned} \quad (8)$$

The characteristic time  $t_c$  is defined as  $t_c = D/U$  and the characteristic strain rate  $\dot{\gamma}_c$  is defined as  $\dot{\gamma}_c = 1/t_c = U/D$ . The characteristic velocity  $U$  is defined by balancing the buoyancy ( $\tau_b = |\Delta\rho|gD$ ) and viscous ( $\tau_v = \tau_y + \mu_p U/D$ ) stresses as

$$U = \frac{|\Delta\rho|gD^2}{\mu_p} - \frac{\tau_y D}{\mu_p}, \quad (9)$$

which includes a contribution of the yield stress. The characteristic viscosity  $\mu_c$  is defined as  $\mu_c = \mu_p + \tau_y/\dot{\gamma}_c$ . It is worth noting that  $\mu_c$  includes the contribution of the yield stress, as recommended by Thompson and Soares (2016). Using this scaling we get the following dimensionless parameters that

describe the problem of interest.

$$\begin{aligned}
 Bo &= \frac{|\Delta\rho|gD^2}{\sigma}, \\
 Fr &= \frac{\rho_1 U^2}{|\Delta\rho|gD} = \frac{\rho_1 U^2}{\tau_y + \mu_p \dot{\gamma}_c}, \\
 Pl &= \frac{\tau_y}{\tau_y + \mu_p \dot{\gamma}_c} = \frac{\tau_y}{|\Delta\rho|gD}, \\
 \mu_r &= \frac{\mu_2}{\mu_c}, \\
 \rho_r &= \frac{\rho_2}{\rho_1}.
 \end{aligned}$$

The Bond number,  $Bo$ , represents the relative importance of the buoyancy force to the capillary force, while the Froude number,  $Fr$ , represents the relative importance of inertial forces to the buoyancy force. It is worth noting that the characteristic velocity may also be written as  $U = \sqrt{Fr|\Delta\rho|gD/\rho}$ . Finally, the plastic number,  $Pl$ , indicates the plastic nature of the fluid, and its value ranges from 0 to 1.  $Pl = 0$  means that the yield stress is zero (Newtonian fluid). In contrast,  $Pl = 1$  implies that the liquid is entirely plastic and remains undeformed. Here,  $Pl = Y_g/3$ , where  $Y_g$  is the yield stress parameters, first defined by Beris et al. (1985). Deoclecio et al. (2021) calculated that bubbles are entrapped in yield stress materials if  $Y_g > 0.20 \pm 0.02$ . Since the viscosity of Fluid 1 is not constant, we define the viscosity ratio,  $\mu_r$ , as the viscosity of Fluid 2 over the characteristic viscosity,  $\mu_c$ . The density ratio  $\rho_r = \rho_2/\rho_1$  is fixed ( $= 0.1$ ) in all the simulations.

The momentum equation can be represented in terms of these dimensionless parameters as

$$\bar{\rho} \left[ \frac{\partial \bar{\mathbf{u}}}{\partial t} + \bar{\mathbf{u}} \cdot \nabla \bar{\mathbf{u}} \right] = -\nabla \bar{P} + \frac{1}{Fr} \nabla \cdot [\bar{\mu} (\nabla \bar{\mathbf{u}} + \nabla \bar{\mathbf{u}}^T)] + \frac{1}{Fr Bo} \bar{\kappa} \mathbf{n} \delta_s - \frac{1}{Fr} \frac{\bar{\rho}}{|1 - \rho_r|} \mathbf{e}_z. \quad (10)$$

In Eq. 10, the plastic number is hidden inside the term  $\bar{\mu} = 1/((1 - \alpha)/\bar{\mu}_1 + \alpha/\bar{\mu}_2)$  where the  $\bar{\mu}_1$  is given as

$$\bar{\mu}_1 = \frac{\mu_1}{\mu_c} = (1 - Pl) \left[ 1 + \frac{Pl}{(1 - Pl)(\bar{\gamma} + \frac{Pl}{N})} \right]. \quad (11)$$

### 3. Code Validation

The numerical simulations are performed using the open-source solver *Basilisk* (Basilisk; Popinet, 2009, 2015; Lagr e et al., 2011). The viscoplastic model of Basilisk solver has been successfully used for complex flows by different researchers (Lagr e et al., 2011; Deka et al., 2019, 2020; Deoclecio et al., 2021).

The mesh dynamically adapts as a function of the volume fraction (tolerance threshold:  $10^{-3}$ )<sup>1</sup>, the velocity field (tolerance threshold:  $10^{-3}$ ), the yield surface (tolerance threshold:  $10^{-2}$ ), and the film region (tolerance threshold:  $10^{-1}$ )<sup>2</sup>. The film region is defined as the region in Fluid 1 located at a distance up to three times the current minimum film thickness,  $h_{min}$ , from both interfaces and above  $z = 0$ . Figure 2 exemplifies mesh adjustment for a drop colliding with an interface, where the image has been mirrored

---

<sup>1</sup>For details about the mesh refinement algorithm, see Popinet (2015)

<sup>2</sup>For the film region, the Basilisk adaptation algorithm is "tricked" to refine the mesh at the maximum refinement level, and any tolerance threshold smaller than 1 is enough.

on the  $z$ -axis. Red lines represent the interfaces. The left side exhibits the mesh, while the right side exhibits the yielded/unyielded (white/black) regions, and the film region (orange) for  $Fr = 200$ ,  $Bo = 20$ ,  $Pl = 0.025$ , and  $\mu_r = 1.0$ . Readers see that the mesh is refined at fluid interfaces, on the yield surface, film region, and the areas with a velocity gradient. All simulations start with a uniform mesh of refinement level<sup>3</sup> 6 across the entire domain, with local refinement around the bubble at the initial maximum level, defined after a convergence test. The maximum refinement level is increased during the film drainage process to reduce the computational cost while still solving the film's flow. The mesh in the film is always at the current maximum level of refinement. The film region is identified by a method based on the signature method of Chirco et al. (2022) to detect thin structures. The software Basilisk automatically sets the time step to obey the  $CFL < 0.5$  condition for simulations with the Volume-of-Fluid model. The maximum timestep is also restricted by the oscillation period  $T$  of the smallest capillary wave  $T = \sqrt{\rho_m \mathcal{D}_{min}^3 / (\pi\sigma)}$ , where  $\rho_m = (\rho_1 + \rho_2)/2$  is the average density and  $\mathcal{D}_{min}$  is the size of the smallest grid element.

Validation tests were carried out to check the solver accuracy, dependency on the grid, and the regularization parameter. They are divided into two parts: first for the rising phenomenon and then for the coalescence phenomenon. For the rising part, we reproduce the steady-state numerical solu-

---

<sup>3</sup>The number of cells per dimension is given by  $2^n$ , where  $n$  is the level of refinement. For example, if a 2D square domain is discretized with a refinement level 8, each direction will contain 256 cells. The whole domain will have 65,536 cells.



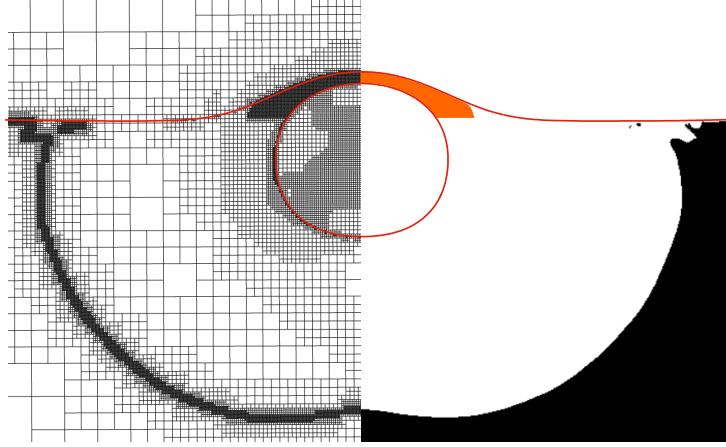


Figure 2: A view of the (left) mesh and (right) yielded/unyielded (black/white) regions and the film (orange) region of a drop impacting on an interface (Obs.: the viscoplastic material inside the film is yielded). The red lines represent the fluid interfaces. The dimensionless parameters are  $Fr = 200$ ,  $Bo = 20$ ,  $Pl = 0.025$ ,  $\mu_r = 1.0$ ,  $\rho_r = 0.1$ , and  $N = 10^5$  with maximum and minimum levels of refinement equal to 12 and 4, respectively.

tion of Dimakopoulos et al. (2013), who simulated rising bubbles using the Augmented Lagrangian Method (ALM) in a Bingham fluid. The dimensionless parameters are  $Bo = 200$ ,  $Fr = 38025$ ,  $Pl = 0.025$ ,  $\mu_r = 0.01$ , and  $\rho_r = 0.01$ . Our definition of  $Bo$  differs from that of Dimakopoulos et al. (2013) since we use the bubble diameter instead of its radius as the characteristic length. Also,  $\mu_r$  and  $\rho_r$  which are equal to zero in Dimakopoulos et al. (2013) (the viscosity and density of the gas phase in the bubble were neglected), but are both equivalent to 0.01 in our simulations. The coalescence part itself is also divided into two parts. First, we reproduce the experimental result of Mohamed-Kassim and Longmire (2003) for the drop impact on a liquid-liquid interface using Newtonian fluids without resolving the flow in the film. The dimensionless parameters are  $Bo = 6.40$ ,  $Fr = 5044$ ,

$Pl = 0.00$ ,  $\mu_r = 0.33$ , and  $\rho_r = 1.189$ . Second, we check the grid dependency to solve the flow in the film and then reproduce the experimental results of Vakarelski et al. (2022) for the shape of the film formed during the impact of a bubble on a solid interface. The dimensionless parameters are  $Bo = 0.228$ ,  $Fr = 5184$ ,  $Pl = 0.00$ ,  $\mu_r = 0.0181$  and  $\rho_r = 0.0012$ .

Fig. 3(a) shows the dimensionless rising velocity of a bubble versus the dimensionless time. The simulation was carried out using the same physical condition used by Dimakopoulos et al. (2013). The maximum mesh refinement levels were 10, 11, 12, and 13 with  $N = 10^5$ . The minimum level for dynamic mesh adaption is kept constant at level 6. Although the velocity profile does not change much while changing the maximum level of refinement from 12 to 13, the computational time increases significantly. Hence, a maximum refinement level of 12 is chosen to perform the rising part of the numerical simulations, which corresponds to a cell size of approximately  $6.10 \times 10^{-3} D$ . Next, we check the value of  $N$  to optimize the computational time without compromising the accuracy or producing numerical instabilities. Figure 3(b) presents the dimensionless velocity profile of the bubble versus the dimensionless time for  $N = 10^2, 10^3, 10^4, 10^5$ , and  $10^6$ , and maximum level of refinement 12. Since the result with  $N = 10^5$  does not change much from the result with  $N = 10^6$ , but the computational time is higher in the latter, we perform the simulations with  $N = 10^5$ . Figure 4 compares our results (right) with  $N = 10^5$  and maximum level of refinement 12 with the numerical solution of Dimakopoulos et al. (2013) (left) for the bubble and yield surface shape. The agreement with the ALM is reasonable for both

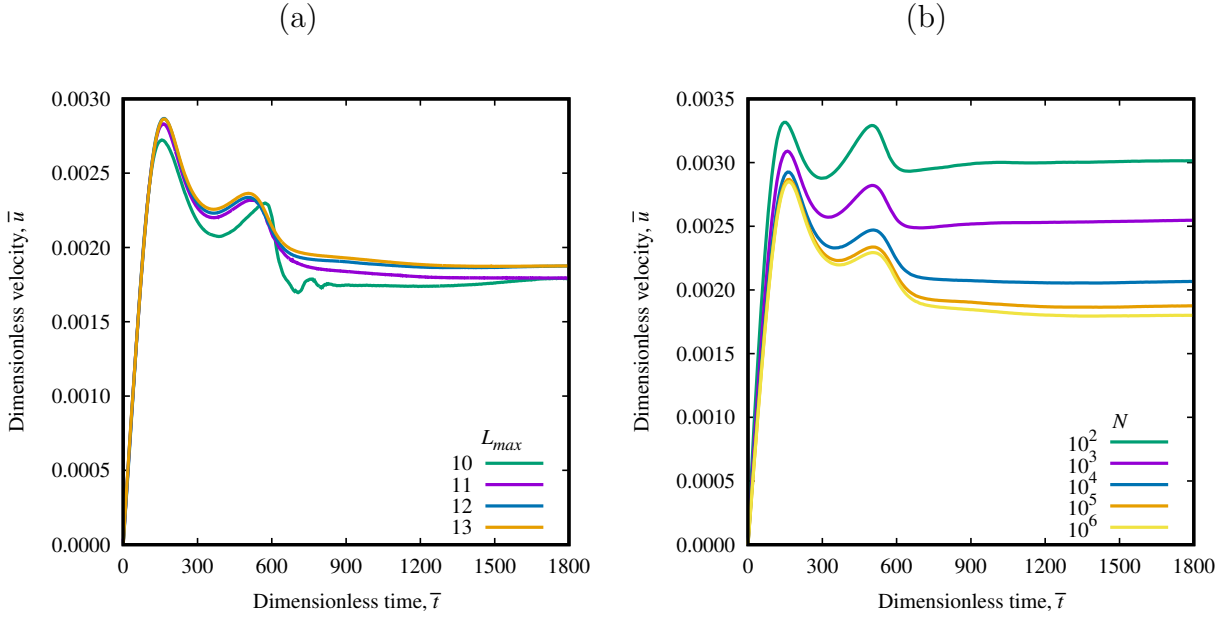


Figure 3: Dimensionless rise velocity,  $\bar{u}$ , with dimensionless time,  $\bar{t}$ , for (a) different mesh maximum refinement levels,  $L_{max}$ , (b) and dimensionless regularization parameters,  $N$ . The minimum refinement level in all cases is 6, while  $L_{max}$  is (a) changed from 10 to 13 in (a) and equal to 12 in (b).  $N = 10^5$  in (a) and changed from  $10^2$  to  $10^6$  in (b). The dimensionless parameters are  $Fr = 38025$ ,  $Bo = 200$ ,  $Pl = 0.025$ ,  $\mu_r = 0.01$ , and  $\rho_r = 0.01$ .

yielded region and the bubble shape.

In the experiment of Mohamed-Kassim and Longmire (2003), the drop is heavier than the surrounding fluid for the coalescence part, and thus the drop falls instead of rising. We inverted the gravity vector's direction ( $\mathbf{e}_z$  is in the positive  $z$ -direction) to account for this in the simulations. As the authors did not assess the inner flow in the draining film, we compare only the position of the fluid-fluid interfaces (outer flow). Here, the mesh is refined only as a function of the volume fraction and velocity fields. We test only

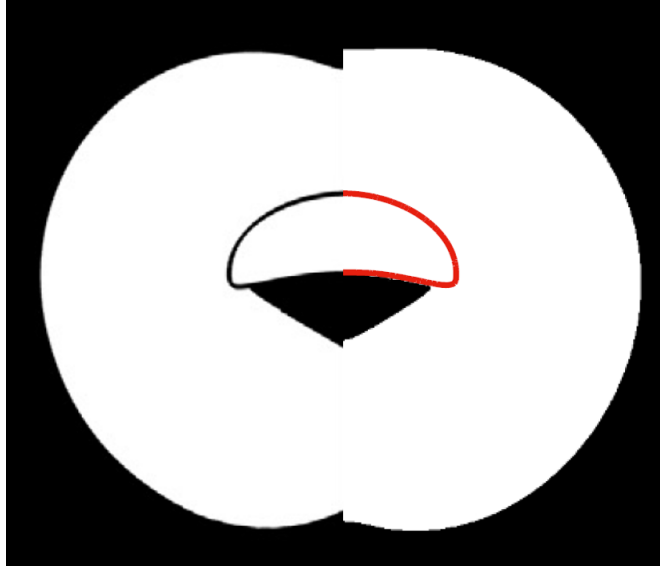


Figure 4: Comparison of our simulation results (right half) with the steady-state solution of Dimakopoulos et al. (2013) using the ALM (left half). The simulations are performed using  $N = 10^5$ ,  $L_{max} = 12$ ,  $Fr = 38025$ ,  $Bo = 200$ ,  $Pl = 0.025$ ,  $\mu_r = 0.01$ , and  $\rho_r = 0.01$ .

the solution dependency on the grid to reproduce the outer flow (the drop collision dynamics). Figure 5 presents the displacement in the  $z$ -direction of a point on the interface initially located at  $(\bar{r}, \bar{z}) = (0, 0)$  (see the yellow square in the insert of Fig. 6) for different mesh maximum refinement levels ( $L_{max} = 10, 11, 12, 13$ , and  $14$ ). Here,  $\bar{t} = 0.0$  designates the time at which the drop nose reaches the interface rest position ( $\bar{z} = 0.0$ ). As can be seen in the figure, the interface position until the first part of the drop rebound ( $\bar{t} \lesssim 200$ ) does not vary much for the different values of  $L_{max}$ . For  $\bar{t} \gtrsim 400$ , the later stage of the drop rebound, the solution does not vary much when changing the maximum level of refinement from 13 to 14. Figure 6 compares the results of Mohamed-Kassim and Longmire (2003) (symbols) for the position

of the drop back (blue circles), drop front (red crosses), and interface (yellow squares) (all at  $r = 0.0$ ) with our simulations (lines) for  $L_{max} = 13$ . Again, there is good agreement between the experimental and numerical results. Hence, a maximum refinement level of at least 13 (cell size of approximately  $3.05 \times 10^{-3} D$ ) is required to reproduce the drop impact dynamics.

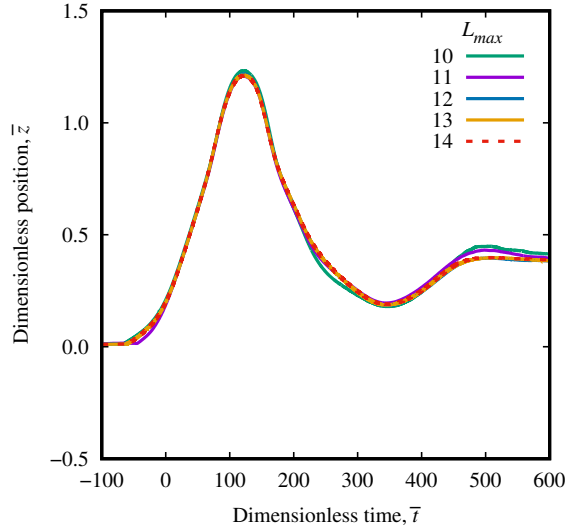


Figure 5: Change of the interface dimensionless position,  $\bar{z}$ , due to a drop impact versus dimensionless time,  $\bar{t}$ , for  $L_{max} = 10, 11, 12, 13$ , and  $14$ . The dimensionless parameters are  $Fr = 5044$ ,  $Bo = 6.40$ ,  $Pl = 0.00$ ,  $\mu_r = 0.33$  and  $\rho_r = 1.189$ .

Although  $L_{max} = 13$  is enough to model the interfaces' positions during the collision step, a higher level of refinement is required to solve the inner flow in the film as the drop approaches the interface, and the thickness of the film decreases. To reduce the computational cost, we perform the drop rising part of the simulations with  $L_{max} = 12$ , and during the drop impact on the top layer interface, we progressively increase  $L_{max}$  to increase the

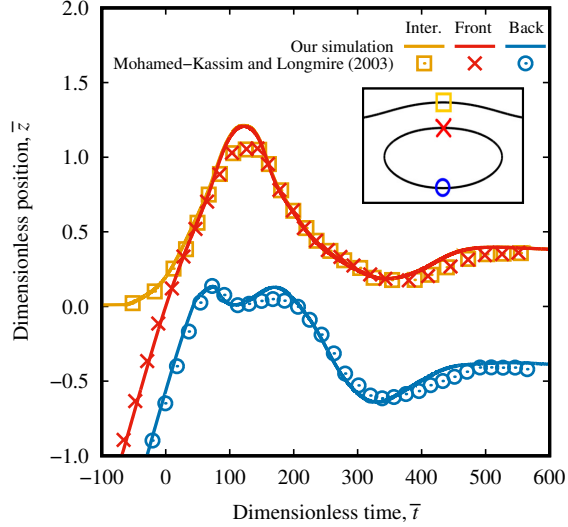


Figure 6: Experimental results of Mohamed-Kassim and Longmire (2003) (symbols) and our simulation (lines) for the drop back (blue) and front (red), and interface (yellow) positions with time. The dimensionless parameters are  $Fr = 5044$ ,  $Bo = 6.40$ ,  $Pl = 0.00$ ,  $\mu_r = 0.33$  and  $\rho_r = 1.189$ , and  $L_{max} = 13$ .

mesh resolution. The maximum level of refinement after the drop impact is taken as a function of the film's minimum thickness,  $h_{min}$ , and the minimum number of cells in the film,  $C$ , according to Eq. 12,

$$L_{max} = \left\lfloor \frac{\log\left(\frac{CH}{h_{min}}\right)}{\log 2} \right\rfloor. \quad (12)$$

Here,  $H = 25D$  is the domain height. We take only the floor integer part of  $L_{max}$ . Figure 7(a) shows the dimensionless minimum film thickness ( $\bar{h}_{min} = h_{min}/D$ ) with dimensionless time ( $\bar{t}$ ) for a drop impacting on a liquid-liquid interface for  $C = 5, 10$ , and  $15$ . The dimensionless parameters are  $Fr = 200$ ,  $Bo = 20$ ,  $Pl = 0.00$  (the surrounding is Newtonian),  $\mu_r = 1.0$ , and  $\rho_r = 0.1$ . Figure 7(b) exhibits the dimensionless film thickness shape ( $\bar{h} = h/D$ ) as

a function of the dimensionless surface length ( $\bar{s} = s/D$ ) at the moment  $\bar{h}_{min} = 0.01$ . As can be seen, the interface is not well represented by  $C = 5$ , in which  $L_{max}(h_{min}) = 13$ . The film shape does change much, varying  $C$  from 10 to 15, with  $L_{max} = 14$  and 15, respectively, but the computational time increases significantly. Here, the interface has a wimple-shaped (Chan et al., 2011), with two minimums, one at the film center and one on the film periphery. The drop and top layer interface shape can be seen in Fig. 8 in the  $(r, z)$  coordinate system (made dimensionless).

We employed  $C = 10$  to numerically produce the film shape ( $\bar{h} \times \bar{r}_b$ ) and bubble center of mass position,  $\bar{z}_{cm}$ , experimental results of Vakarelski et al. (2022). The results are shown in Fig. 9(a) and (b), respectively. There is good agreement between the experimental and numerical results. Therefore, we select  $C = 10$  for our simulations, which requires a maximum refinement level of 14 at  $\bar{h}_{min} = 0.01$ .

In summary, we chose  $N = 10^5$ ,  $L_{max} = 12$  for the rising part, and  $L_{max}$  increasing gradually from 12 up to 14 as a function of  $h_{min}$  after the drop impact. Thus, the film's minimum number of cells,  $C$ , is equal to 10. Due to the high computational cost of performing systematic simulations for  $\bar{h}_{min} < 0.01$ , the computational drainage time,  $\Delta t$ , is taken as the time elapsed between  $\bar{h}_{min}$  thins from 0.1 to 0.01.

#### 4. Results and discussion

This section discusses drop coalescence dynamics in viscoplastic materials and compares them to the Newtonian case. The drop rise and collision

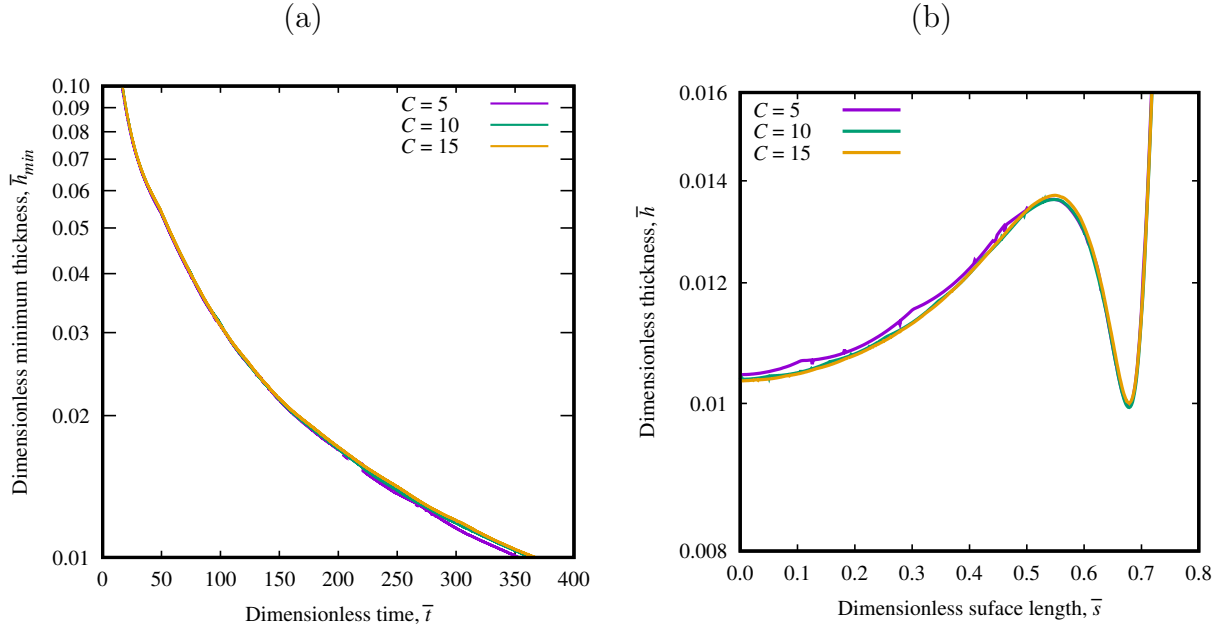


Figure 7: (a) Dimensionless minimum film thickness,  $\bar{h}_{min}$ , versus Dimensionless time,  $\bar{t}$ , and (b) dimensionless film thickness  $\bar{h}$  versus dimensionless surface length  $\bar{s}$  for  $C = 5, 10$ , and  $15$  at the moment  $\bar{h}_{min} = 0.01$ . Results for  $Fr = 200$ ,  $Bo = 20$ ,  $Pl = 0.00$ ,  $\mu_r = 1.0$ , and  $\rho_r = 0.1$ .

dynamics are taken taking into account, and the dimensionless computational drainage time,  $\Delta\bar{t}$ , is used to give a measure (an indication) of how the yield stress affects the coalescence time. We begin our discussion by assessing the effects of the governing dimensionless numbers ( $Fr$ ,  $\mu_r$ ,  $Bo$ , and  $Pl$ ) on drop rise (Sec. 4.1). Then, in the sequence, we investigate their effect on drop collision and on  $\Delta\bar{t}$ , first for Newtonian surroundings (Sec. 4.2) and then introducing plasticity (Sec. 4.3).



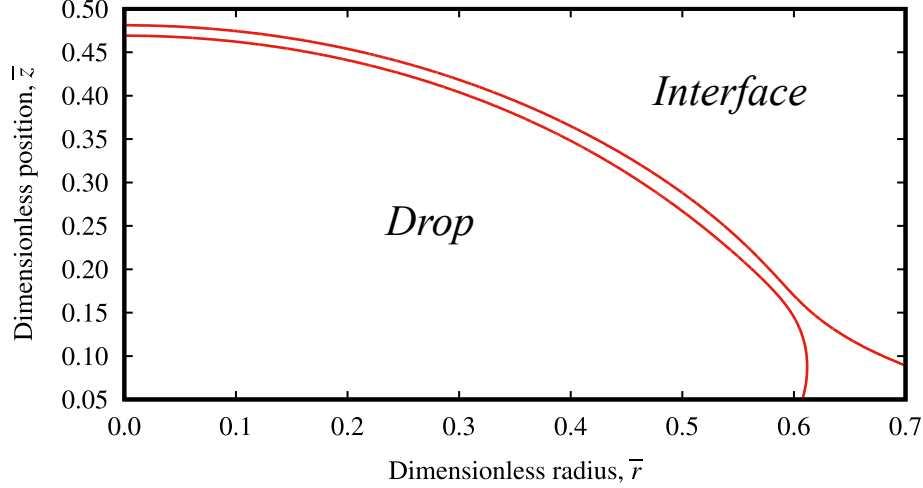


Figure 8: Drop collision on the top layer interface and the entrapped film in the  $(r, z)$  coordinate system with for  $C = 10$  at the moment  $\bar{h}_{min} = 0.01$ . Results for  $Fr = 200$ ,  $Bo = 20$ ,  $Pl = 0.00$ ,  $\mu_r = 1.0$ , and  $\rho_r = 0.1$ .

#### 4.1. Drop rise

The drop velocity and shape during the rise stage are among the main parameters influencing the coalescence process. The collision of a drop with a larger width and a higher impact velocity (which causes a more considerable width increase during the collision stage) leads to a draining film with a more significant length, which tends to slow down the film drainage process (Zawala and Malysa, 2011; Kočárková et al., 2013). The interdependence between the drop velocity and shape and the different effects of the interplaying forces make drop rise a complex phenomenon. The drop deformation depends on the balance between the surface tension force, which tends to preserve the drop's spherical shape and the distorting forces (*e.g.*, inertial

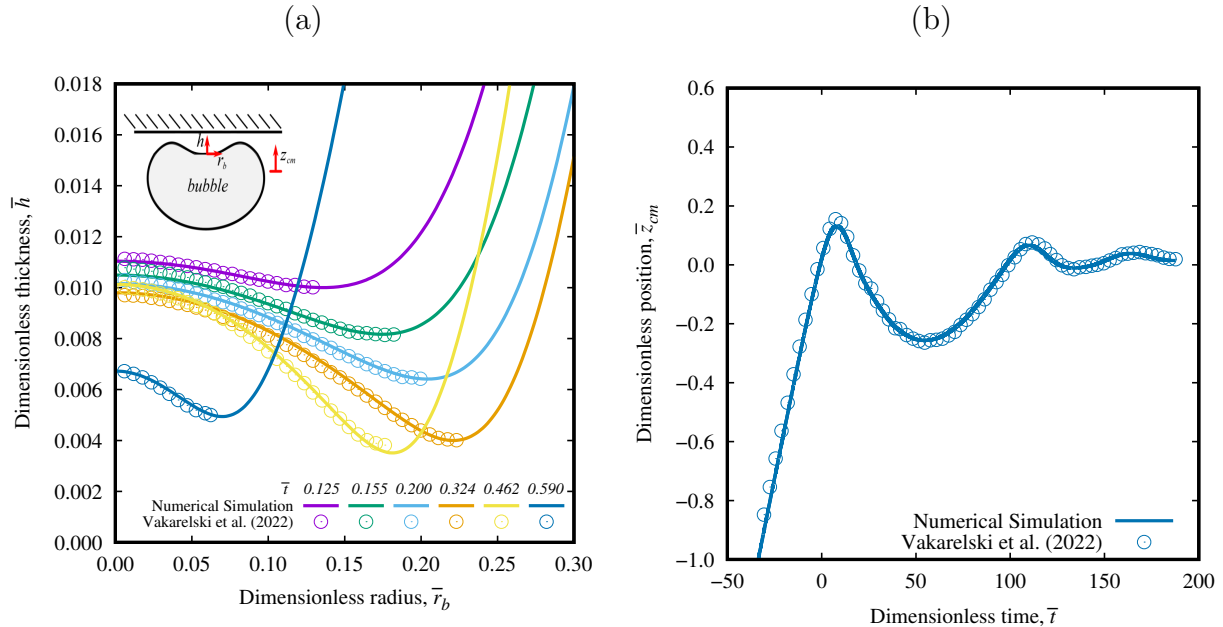


Figure 9: (a) Dimensionless film thickness,  $\bar{h}$ , with dimensionless film radius,  $\bar{r}_b$ , at different times for an air bubble impacting on a solid surface experimental results of Vakarelski et al. (2022) (open circles) and our numerical results (solid lines). (b) Bubble center of mass dimensionless position,  $\bar{z}_{cm}$ , with dimensionless time,  $\bar{t}$ , experimental (open circles) and numerical (solid lines) results. The dimensionless parameters are  $Fr = 5184$ ,  $Bo = 0.089$ ,  $Pl = 0.00$ ,  $\mu_r = 0.0181$  and  $\rho_r = 0.0012$ , and  $L_{max} = 14$ .

and plastic forces) compete with each other to deform the drop in different ways. In this section, we first discuss the general effects of  $Fr$ ,  $\mu_r$ , and  $Pl$ , on drop rise velocity and shape since these express the relative importance of the distorting forces only. Then, the effect of  $Bo$ , which includes the shape-persevering surface tension force, is discussed for flows dominated by buoyancy (low values of  $Pl$ ) and plastic (high values of  $Pl$ ) effects. Since  $Bo$  give a measure of the drop deformability (the ease with which the distorting forces deform the drop), its effect on the drop velocity and shape depends on

the dominating distorting force.

Figure 10(a) and (b) exhibit drop dimensionless terminal velocity (multiplied by  $Fr^{1/2}$  to remove the dependency of  $U$  on  $Fr$ ),  $\bar{u}_t$ , and drop dimensionless terminal width (which gives a measure of the drop deformation),  $\bar{D}_{tW} = D_{tW}/D$ , respectively, as a function of  $Pl$ , for different values of  $Fr$ ,  $\mu_r$ , and  $Bo$ . We take the purple line with squares ( $Fr = 200$ ,  $\mu_r = 0.1$ , and  $Bo = 2$ ) in Fig. 10 as the base scenario. Then, we change  $Fr$ ,  $\mu_r$ , and  $Bo$  one at a time to evaluate their effects on drop rise velocity and shape. To assist in the discussion about drop deformation in the rise stage, Fig. 11 exhibits the drop shape at steady-state rise for some combinations of the dimensionless parameters in Fig. 10. Figure 10(a) indicates that an increase in the Froude number from 200 (purple line) to 2000 (yellow line) increases the drop terminal velocity. Such a fact is explained by increased inertial forces relative to viscous forces. In the dimensional analyses, viscous forces scale with the buoyant force. Thus, an increase in  $Fr$  also increases inertial forces relative to viscous forces. As a consequence, the drop width also increases with  $Fr$  (see Fig. 10(b)) since the higher dynamic pressure in front of the drop tends to distort it to an oblate shape ( $\bar{D}_{tW} > 1$ ). The increase of the drop width can be observed by comparing Fig 11(a) purple and yellow lines for  $Pl = 0.00$ ,  $\mu_r = 0.1$ ,  $Bo = 2$ , and  $Fr = 200$  and 2000, respectively. The viscosity ratio has the opposite effect of that of the Froude number. It enhances viscous dissipation and tends to reduce drop terminal velocity, as indicated by the blue line (compared to the purple line) in Fig. 10(a) for  $\mu_r = 10$ . As a result, the drop width slightly reduces, as shown in Fig. 10(b) and as can be seen by comparing Fig 11(a) purple and blue lines, for  $Pl = 0.00$ ,  $Bo = 2$ ,  $Fr = 200$ ,

and  $\mu_r = 0.1$  and 10, respectively.

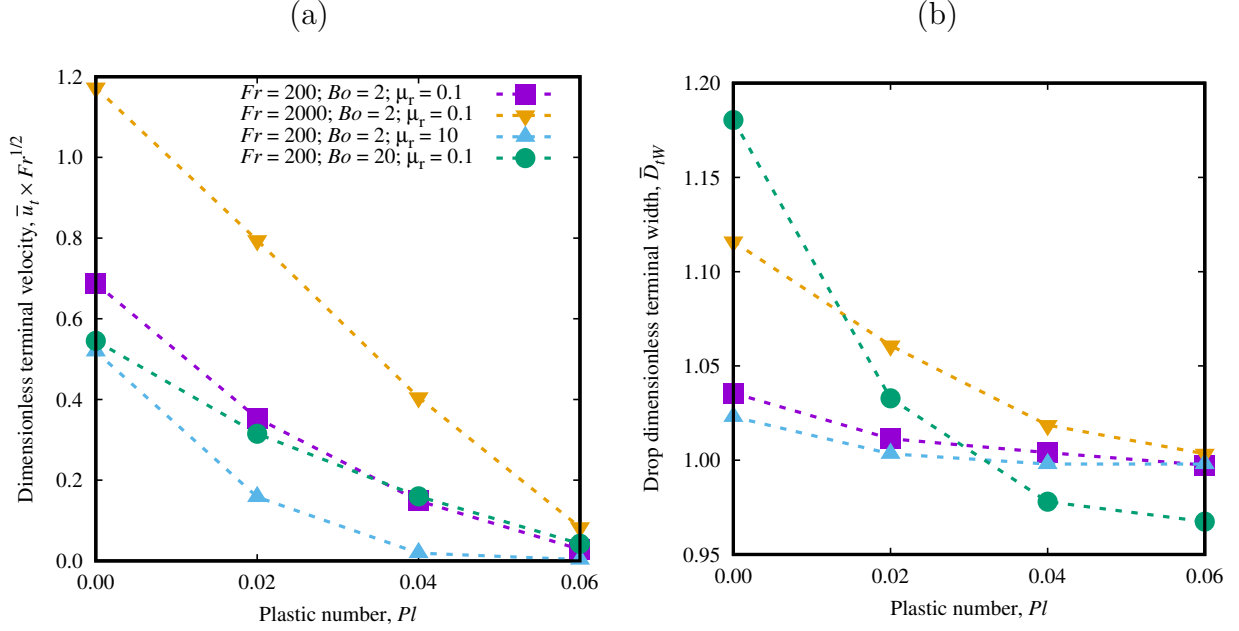


Figure 10: (a) Drop dimensionless terminal velocity,  $\bar{u}_t (\times Fr^{1/2})$  and (b) drop dimensionless terminal width,  $\bar{D}_{tW}$ , versus the plastic number,  $Pl$ .

Figure 10 also shows that an increase in the plastic number tends to reduce both  $\bar{u}_t$  and  $\bar{D}_{tW}$ . Whenever inside a viscoplastic material, drops rise inside an envelope of yielded material that decreases in size with an increment in plasticity (Deoclecio et al., 2021; Tsamopoulos et al., 2008). Therefore, the drop movement becomes more restricted with an increase in  $Pl$ . It is to be noted that  $Pl = 0.06$  gives  $Y_g = 0.18$  (Deoclecio et al., 2021), which is close to the drop entrapment condition. The yield stress has a dual nature, plastic and viscous (Thompson and Soares, 2016), and a change in  $Pl$  only changes the contribution of the yield stress to the total stress (*e.g.*,  $\tau_c = \tau_y + \mu_p \dot{\gamma}_c$ ),

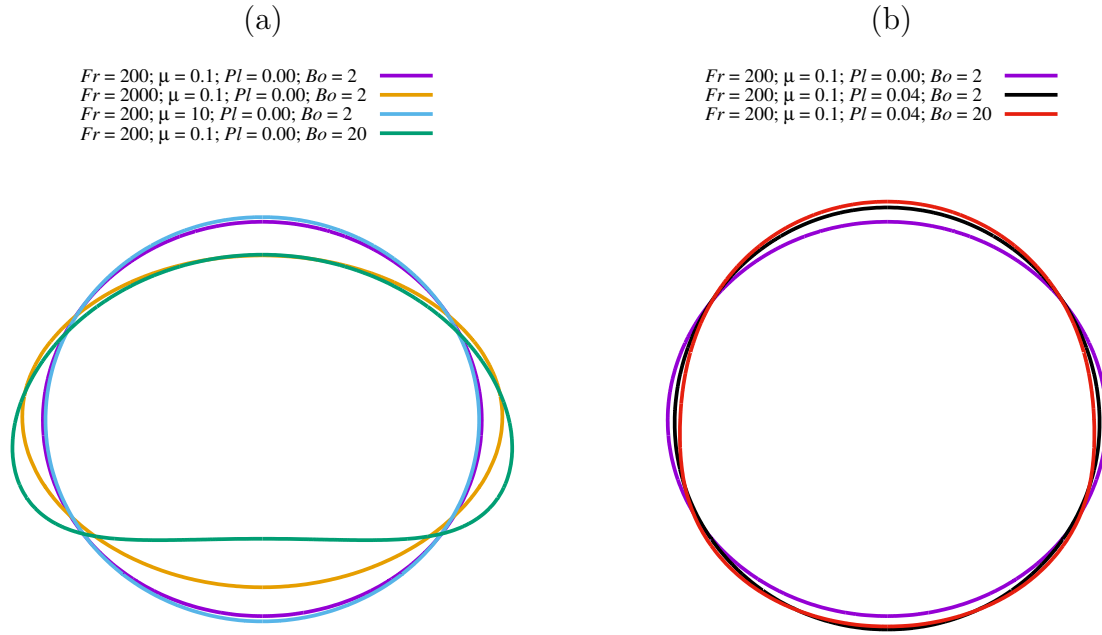


Figure 11: Drop shape at steady-state rise for different sets of dimensionless parameters.

but not the total stress itself. Hence, for a fixed  $Fr$ , this velocity reduction and movement restriction should predominantly be due to plastic effects and not an increase in viscous effects. The drop width reduction with  $Pl$  does not occur only because of the drop velocity reduction (which reduces the dynamic pressure in front of the drop). Plastic effects act against the surface tension force to form prolate drops ( $\bar{D}_{tW} < 1$ ). Such prolate drops may be explained by the viscosity field of the surrounding Bingham material, which is shear thinning (*e.g.*,  $\mu_1 = \mu_p + \tau_y / \|\dot{\gamma}\|$  and an increase in  $\|\dot{\gamma}\|$  causes a decrease in  $\mu_1$ ). Figure 12 exhibits the yielded/unyielded (white/black) regions around a rising drop (left) and the surrounding Bingham material viscosity field (right) for  $Pl = 0.06$ ,  $Fr = 200$ ,  $Bo = 20$ , and  $\mu_r = 0.1$ . The viscoplastic material viscosity is smaller on the drop poles than on the

drop equator. As a result, drops tend to acquire a more prolate shape to penetrate the viscoplastic material through the lower viscosity region. This is in agreement with the numerical results of Tsamopoulos et al. (2008). The authors simulated steady-state rising bubbles in viscoplastic materials using the Papanastasiou model (*i.e.*, a regularized version of the Bingham model). They calculated the strain rate near the bubble equator and the bubble poles and found that the strain rate near the bubble equator was meager compared to the strain rate near the bubble poles. Consequently, the bubble elongates in the direction of its poles. The black line of Fig. 11(b) shows the drop shape for the exact parameters of the drop in with purple line (which is the same drop represented by the purple line in Fig. 11(a)), except for  $Pl = 0.04$ . The shape of the former is close to a sphere ( $\bar{D}_{tW} \approx 1$ ), while the latter is slightly oblate ( $\bar{D}_{tW} \gtrsim 1$ ).

An increasing  $Bo$  tends to enhance the deformation caused by the dominating distorting force, and a reducing  $Bo$  tends to approximate the drop shape to that of a sphere. Therefore, for low values of  $Pl$ , in which buoyancy effects dominate over plastic effects, drops tend to acquire a more oblate shape (an increase in  $\bar{D}_{tW}$ ) with an increase in  $Bo$ . This can be seen by comparing the purple and green lines in Fig. 10(b) for  $Pl \leq 0.02$ ,  $Fr = 200$ ,  $\mu_r = 0.1$ , and  $Bo = 2$  and  $20$ , respectively. The effect of an increase in the Bond number on drop shape for low values of  $Pl$  can also be observed by comparing Fig. 11(a) purple and green lines for  $Pl = 0.00$ ,  $\mu_r = 0.1$ ,  $Fr = 200$ , and  $Bo = 2$  and  $20$ , respectively. Since the drop width increases with  $Bo$ , the drop velocity decreases due to its larger cross-sectional area, as shown by the purple and green lines in Fig. 10(a).

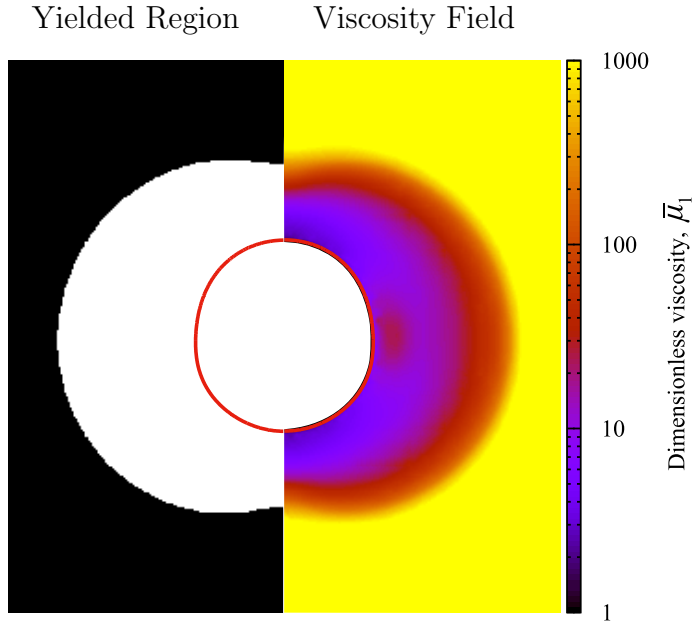


Figure 12: Yielded/unyielded (white/black) regions (left) and dimensionless viscosity field,  $\bar{\mu}_1$ , (right) for a drop at steady-state rise,  $Pl=0.06$ ,  $Fr = 200$ ,  $Bo = 20$ , and  $\mu_r = 0.1$

For high values of  $Pl$ , plastic effects are dominant, and the drop shape becomes more prolate with an increase in  $Bo$  (a decrease in  $\bar{D}_{tW}$ ). This is shown by the purple and green lines in Fig. 10(b) for  $Pl \geq 0.04$ . The drop shape change when increasing  $Bo$  for high values of  $Pl$  is depicted in Fig. 11(b) black and red lines for  $Pl = 0.04$ ,  $\mu_r = 0.1$ ,  $Fr = 200$ , and  $Bo = 2$  and 20, respectively, where the latter is shown to be more prolate than the former. As a result of the width reduction, the drop velocity increases when increasing the Bond number, which can be seen by comparing the purple and green lines in Fig. 10(a) for  $Pl \geq 0.04$ .

#### 4.2. Drop collision and $\Delta\bar{t}$ in Newtonian materials

Drop velocity and shape change during the impact on the top layer interface, together with the rheological properties of the fluids, govern the coalescence process. This section evaluates the effects of  $Fr$ ,  $\mu_r$ , and  $Bo$  on drop collision dynamics (velocity and shape change) and computational drainage time in Newtonian surroundings. Figure 13(a) and (b) present the dimensionless drop velocity (multiplied by  $Fr^{1/2}$ ),  $\bar{u}$ , and dimensionless width,  $\bar{D}_W$ , respectively, versus dimensionless time (divided by  $Fr^{1/2}$ ),  $\bar{t}$ , for  $Pl = 0.00$  and the same sets of the other of dimensionless parameters of Fig. 10. The black dashed vertical line marks the time  $\bar{t} = 0.0$  when the dimensionless minimum distance between the drop and the interface is  $\bar{h}_{min} = 0.1$ , and the colored dashed vertical lines mark the time  $\bar{t}$  at which  $\bar{h}_{min} = 0.01$ . We take the purple line in Fig. 13 (for  $Fr = 200$ ,  $\mu_r = 0.1$ , and  $Bo = 2$ ) as the base case, and then change  $Fr$ ,  $\mu_r$ , and  $Bo$  one at a time. Moreover, two auxiliary figures aid in the discussion, Fig. 14 and 15. Fig. 14 shows the drop and top layer interface shape for  $\bar{h}_{min} = 0.1, 0.05$ , and  $0.01$  (the film thinnest part is marked by a pair of black arrows), and Fig. 15 shows the draining film shape for  $\bar{h}_{min} = 0.01$ .

In general, Fig. 13 shows that as the drop approaches the top layer interface, its velocity decreases, and its width increases due to the conversion of kinetic energy to surface energy. Then, the drop eventually retracts back and rebounds. In the process, part of the kinetic energy is dissipated by viscous effects. In the case of increasing the Froude number (purple line for  $Fr = 200$  and yellow line for  $Fr = 2000$ ), the drop impact velocity increases, and as a result, the drop width during the collision stage also increases. The



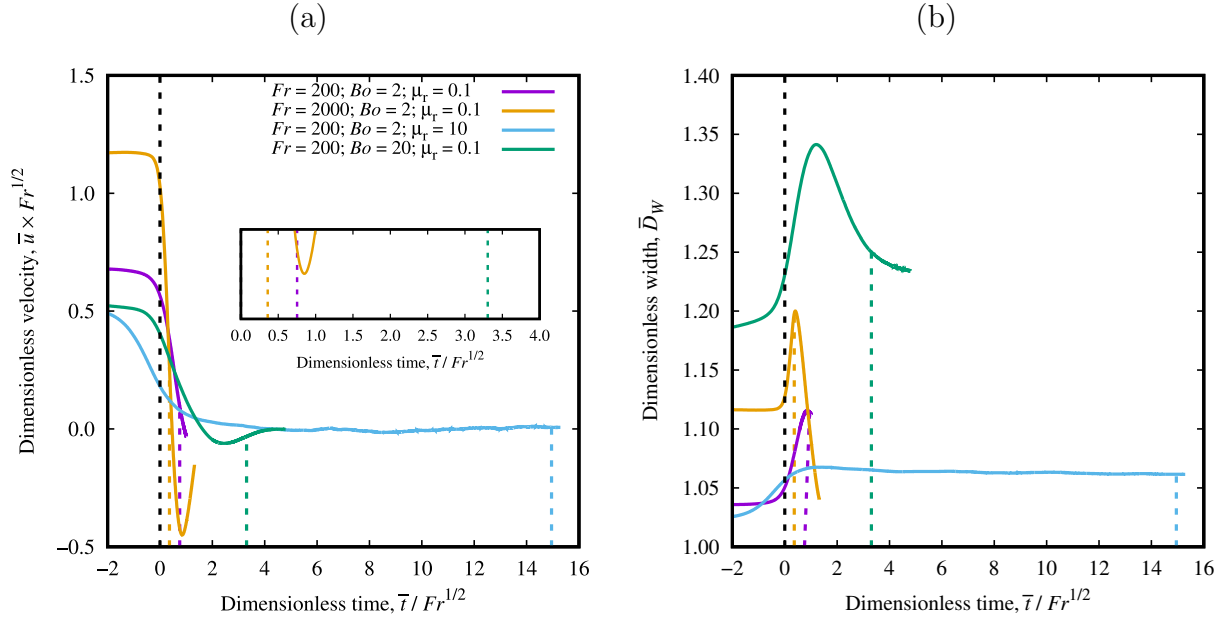


Figure 13: Drop (a) dimensionless velocity,  $\bar{u}$  ( $\times Fr^{1/2}$ ), and (b) dimensionless width,  $\bar{D}_{tW}$ , versus dimensionless time,  $\bar{t}$  ( $/ Fr^{1/2}$ ). The dimensionless parameters are  $Pl = 0.00$ , (purple line)  $Fr = 200$ ,  $\mu_r = 0.1$ ,  $Bo = 2$ , (yellow line)  $Fr = 2000$ ,  $\mu_r = 0.1$ ,  $Bo = 2$ , (blue line)  $Fr = 200$ ,  $\mu_r = 10$ ,  $Bo = 2$ , and (green line)  $Fr = 200$ ,  $\mu_r = 0.1$ ,  $Bo = 20$ .

higher impact energy leads to a more considerable pressure build-up in the film and a more extensive deformation of the interfaces. As a result, the film length is more prominent for  $Fr = 2000$  than for  $Fr = 200$ . This can be seen by comparing the drop and top layer interface shape in Fig. 14(a) and (b) for  $Fr = 200$  and 2000, respectively, and the film shape shown by the purple and yellow lines in Fig. 15 for  $Fr = 200$  and 2000, respectively. For  $Fr = 200$ , the film is spherical, but for  $Fr = 2000$ , it is dimpled due to the higher pressure build-up. Although a larger film length tends to slow down the drainage process, a decrease in the computational drainage time is

observed for an increase in the Froude number. As discussed in the previous section, an increase in the Froude number increases the rising velocity due to the reduction of viscous forces relative to inertial forces. Therefore, the decrease in resistive viscous effects seems to overcompensate for the increase in inertial effects (which tend to increase the film length) for the range of parameters studied. In both cases, the simulation drainage time stopping criterion ( $\bar{h}_{min} = 0.01$ ) is reached while the drops are still colliding (bouncing: the impact energy has not been fully dissipated by viscous effects) on the interface. The occurrence of coalescence while bouncing on the interface was observed experimentally by Zawala and Malysa (2011), and Vakarelski et al. (2019) for bubbles in high-purity water.

Regarding the viscosity ratio effect, Fig. 13 shows that in the case of increasing  $\mu_r$  from 0.1 (purple line) to 10 (blue line), the drop velocity and width change during the collision stage occurs more slowly. Due to the higher viscous dissipation, the kinetic to surface energy transfer rate is reduced, and Fig. 13(b) shows that the drop width increase is less for  $\mu_r = 10$  than for  $\mu_r = 0.1$ . Viscous dissipation dampens (smooths and slows down) the collision process, and as a result, the drop does not rebound (its velocity monotonically decreases to zero). Despite the smaller width and impact velocity, the drainage time increases significantly with the viscosity ratio increase. The drop stays mostly after the collision virtually static ( $\bar{u} \approx 0$ ), resting on the interface, while the draining of the film proceeds. Vakarelski et al. (2019) observed a similar behavior experimentally. The authors assessed the effects of interface mobility on the interfacial coalescence of

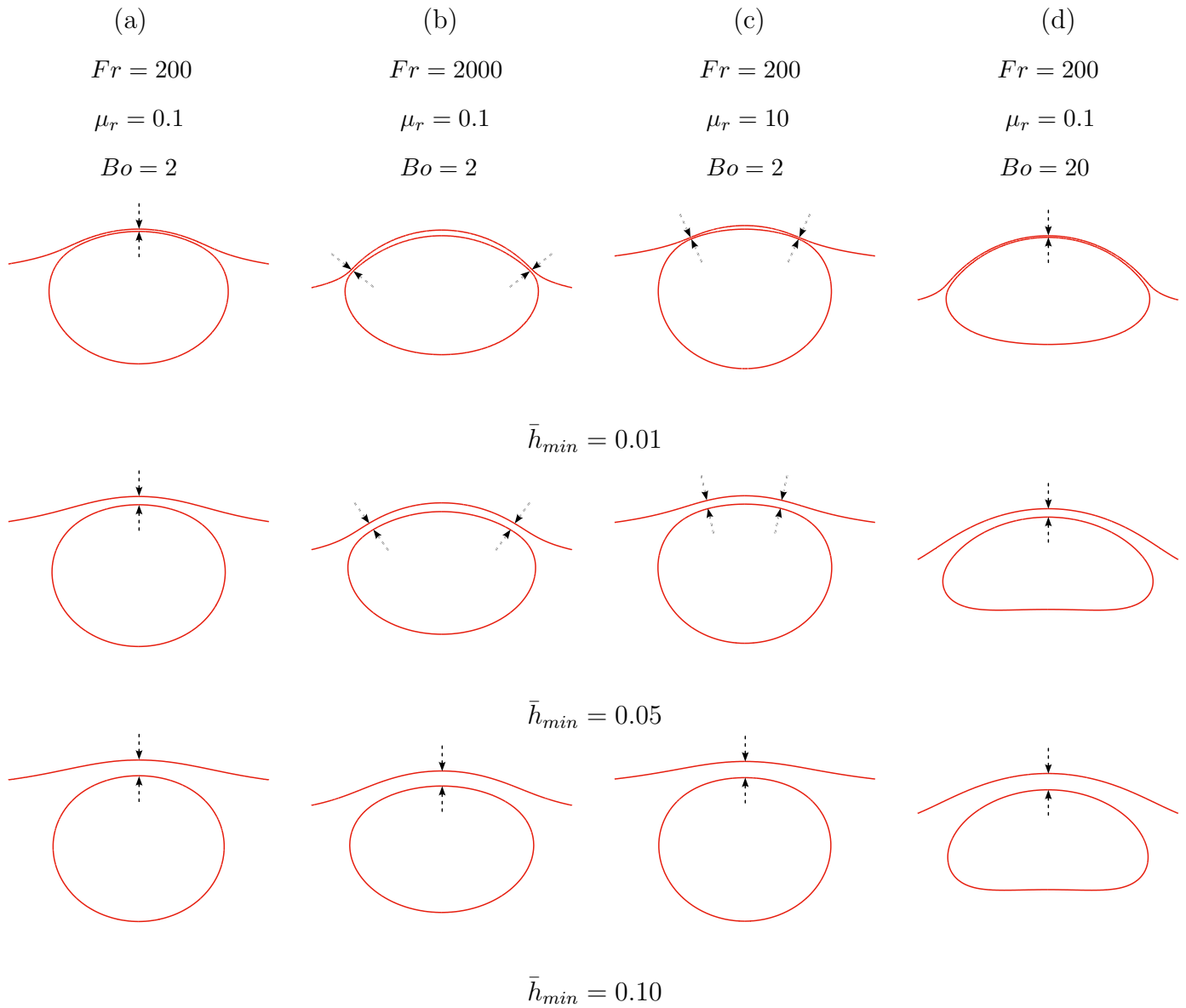


Figure 14: Drop and top layer interface shape for  $\bar{h}_{min} = 0.10$  (third row),  $\bar{h}_{min} = 0.05$  (second row), and  $\bar{h}_{min} = 0.01$  (first row) for  $Pl = 0.00$  and (a)  $Fr = 200$ ,  $Bo = 2$ , and  $\mu_r = 0.1$ , (b)  $Fr = 2000$ ,  $Bo = 2$ , and  $\mu_r = 0.1$ , (c)  $Fr = 200$ ,  $Bo = 2$ , and  $\mu_r = 10$ , and (d)  $Fr = 200$ ,  $Bo = 20$ , and  $\mu_r = 0.1$ . The film thinnest part is marked by a pair of black arrows.

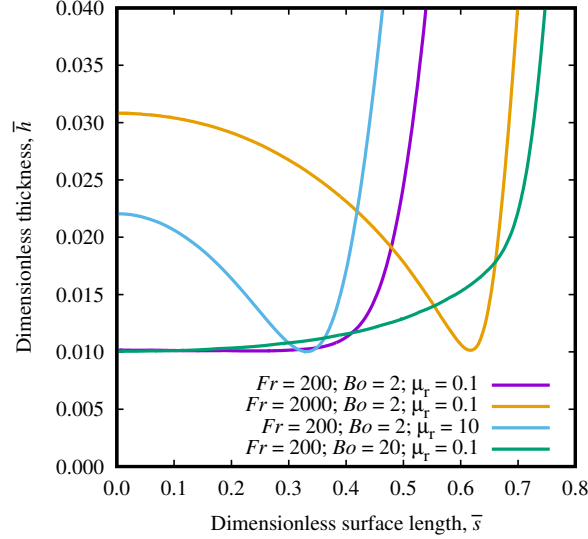


Figure 15: Film dimensionless thickness,  $\bar{h}$ , versus dimensionless surface length,  $\bar{s}$ , at  $\bar{h}_{min} = 0.01$ . The dimensionless parameters are  $Pl = 0.00$ , (purple line)  $Fr = 200$ ,  $\mu_r = 0.1$ ,  $Bo = 2$ , (yellow line)  $Fr = 2000$ ,  $\mu_r = 0.1$ ,  $Bo = 2$ , (blue line)  $Fr = 200$ ,  $\mu_r = 10$ ,  $Bo = 2$ , and (green line)  $Fr = 200$ ,  $\mu_r = 0.1$ ,  $Bo = 20$ .

bubbles. The coalescence time of mobile-surface bubbles was much less than that of immobile-surface bubbles; however, the bouncing amplitude of the former was more significant than the latter. For mobile-surface bubbles, a substantial drop rebound was followed by rapid coalescence. Similar behavior was observed for the lower viscosity ratio cases (purple and yellow lines), where the film hydrodynamics boundary condition is closer to the bubble with an mobile surface.  $\bar{h}_{min} = 0.01$  is reached while the drops are still bouncing on the interface. For the immobile-surface bubbles, the bouncing was weaker, but the bubble stood on the interface for a longer time before coalescing. This behavior is similar to our higher viscosity ratio case, where

the film hydrodynamics boundary condition is closer to the bubble with an immobile surface. Vakarelski et al. (2019) argue that these behaviors are due to the more negligible viscous dissipation of the mobile-surface case, which allows for a more extensive conversion of kinetic to surface energy (stronger rebounding) but also faster drainage. Therefore, the film quickly reaches small thicknesses for the lower viscosity ratio while the drop bounces (collides) on the interface. Conversely, for the higher viscosity ratio, the film thinning during the collision stage is small. As a result, a more significant portion of the drainage process occurs during the resting stage, while the drop is virtually static. Furthermore, the larger drop and top layer viscosity lead to a stronger pressure gradient in the film. Such a mechanism forms a dimple-shaped film, making the drainage process even more difficult due to the restricted flow passage on the film periphery. The formation of dimpled films due to the coupling of hydrodynamics forces and interface deformation is also predicted by the lubrication theory (Chan et al., 2011). Figure 14(c) and the blue line in 15 show that for  $\mu_r = 10$  the film becomes dimpled, while for  $\mu_r = 0.1$  (Fig. 14(a) and purple line in Fig. 15) the film is spherical. Such behavior agrees with the results of Aarts and Lekkerkerker (2008) and Chi and Leal (1989). The former observed experimentally that film rupture tended to occur at the film center (spherical-shaped film) and film periphery (dimple-shaped film) during the interfacial coalescence of bubbles (low levels of viscosity ratios) and drops (high levels of viscosity ratios), respectively. The numerical results of Chi and Leal (1989) also indicate that increasing the viscosity ratio tends to slow down the drainage process and make the film acquire a dimpled-shape. Therefore, an increase in  $\mu_r$  increases the

drainage time due to an increasing viscous dissipation and the change in the film boundary condition by the rheological properties of the inner phase.

Lastly, in the case of an increase in the Bond number from 2 (purple line) to 20 (green line), the drop width increases in both the rise and collision stages. Here, the viscosity of both phases is kept constant. As a result, the film length increases, as depicted in Fig. 14(d) and by the green line in Fig. 15. Since the buoyancy force acting on the drop is distributed over a more significant film area, the pressure in the film decreases, and the drainage process slows down. For  $Bo = 20$ , the drop has time to nearly complete one rebound before  $\bar{h}_{min} = 0.01$ , while for  $Bo = 2$ , it does not. For small values of the Bond number, surface tension is dominant, and the drop is less deformed by the distorting forces. As a result, a smaller film is formed, facilitating the film-thinning process. The results agree with the experimental results Kočárková et al. (2013), who experimentally measured the thinning rate of thin films created during the interfacial coalescence of gas bubbles in Newtonian liquids. Furthermore, the authors verified that the drainage time is a function of the film length (or film area), a function of the Bond number.

In summary, for Newtonian surroundings, an increase in  $Fr$  tends to reduce the drainage time due to the reduction of viscous effects relative to inertial effects, despite the drop's larger width and higher impact velocity. An increase in  $\mu_r$  has the opposite effect. It increases the drainage time, despite the reduction in drop width and impact velocity. In addition, it contributes to the formation of dimpled films, which are harder to drain. A higher drop and top layer viscosity also smooth the collision process, causing the drainage process occurring during the drop collision and resting stages

to lose and gain significance, respectively. Lastly, an increase in  $Bo$  tends to enlarge the film length, which increases the drop rebound amplitude and the drainage time.

#### 4.3. Drop collision and $\Delta\bar{t}$ in Bingham materials

Plastic effects add extra complexity to the already complex coalescence phenomenon. Therefore, this section is divided into two parts to facilitate the discussion. First, we assess the influence of plastic effects on the drop collision dynamics (drop velocity and shape) in Sec. 4.3.1, and second, we discuss the impact of  $Pl$  on  $\Delta\bar{t}$  in Sec. 4.3.2.

##### 4.3.1. Drop collision in Bingham materials

In this section, we discuss plastic effects on drop collision dynamics. First, we vary the plastic number while the other parameters are kept constant. Then, we investigate how changes in  $Fr$ ,  $\mu_r$ , and  $Bo$  affect drop collision for flows dominated by plastic effects.

Figure 16(a) and (b) present the dimensionless drop velocity (multiplied by  $Fr^{1/2}$ ),  $\bar{u}$ , and dimensionless width,  $\bar{D}_W$ , respectively, versus dimensionless time (divided by  $Fr^{1/2}$ ),  $\bar{t}$ , for  $Fr = 200$ ,  $Bo = 20$ ,  $\mu_r = 0.1$ , and  $Pl = 0.00, 0.02, 0.04, \text{ and } 0.06$ . The black dashed line marks the time  $\bar{t} = 0.0$  at which  $\bar{h}_{min} = 0.1$ , and the colored dashed lines mark the time at which  $\bar{h}_{min} = 0.01$  (we leave the discussion about  $\Delta\bar{t}$  to the next section). Furthermore, auxiliary Fig. 17 and 18 (described in the sequence), assist in the assessment of plastic effects on drop collision dynamics. For the Newtonian surrounding (purple line in Fig. 16), the drop velocity and width monotonically decrease and increase, respectively, as it approaches the top layer

interface. However, a different behavior is observed for the viscoplastic cases (yellow, blue, and green lines). The drop velocity and width increase and decrease, respectively, while approaching the interface. This behavior may be explained by the interaction between the drop and the interface before the collision moment. To exemplify this, Fig. 17 presents snapshots of a drop and the yield surface around it during the rise, collision, and resting stages for  $Pl = 0.04$ ,  $Fr = 200$ ,  $Bo = 20$ , and  $\mu_r = 0.1$  (blue line in Fig. 16). Figure 17(a) shows the drop rising at steady-state and surrounded by an envelope of yielded material. As the drop approaches the top layer fluid (Fig. 17(b) and (c)), the latter starts to deform, aiding in the yielding of the surrounding material in front of the drop. With the increase of the yielded region in this area, the drop rise velocity increases, and its width reduces as it approaches the interface. Eventually, as the drop collision proceeds, kinetic energy is converted to surface energy, and the drop width increases, as depicted by Fig. 17(d), (e), and (f). In Fig. 17(f), the drop is approaching the resting stage ( $\bar{u} \approx 0.0$ ), in which it rests on the interface (almost static) as the drainage process goes on and the size of the yield envelope decreases. Besides the kinetic and surface energy conversion, the buoyancy force pressing the drop against the interface also contributes to this increase in the drop width.

Figure 18 shows the drop and top layer interface shape for each condition in Fig. 16 at the moment  $\bar{h}_{min} = 0.10, 0.05, \text{ and } 0.01$  (the film thinnest part is marked by a pair of black arrows). As can be seen, the drop width reduction is enhanced by an increase in the plastic number, resulting in a shortening of



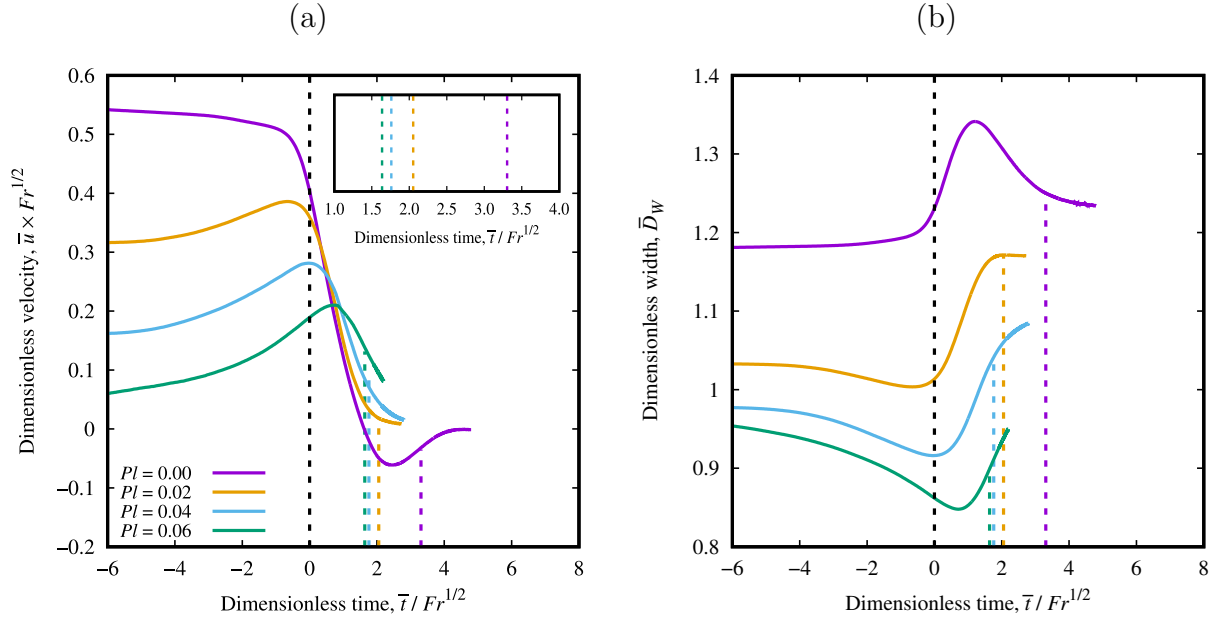


Figure 16: Drop (a) dimensionless velocity,  $\bar{u}$  ( $\times Fr^{1/2}$ ), and (b) dimensionless width,  $\bar{D}_{tW}$ , versus dimensionless time,  $\bar{t}$  ( $/ Fr^{1/2}$ ). The dimensionless parameters are  $Fr = 200$ ,  $Bo = 20$ ,  $\mu_r = 0.1$ , and  $Pl = 0.00$  (purple line),  $0.02$  (yellow line),  $0.04$  (blue line), and  $0.06$  (green line).

the film's length. Figure 18 also conveys that plasticity makes the film more spherical. The tendency to form spherical-shaped films with an increase in the level of plasticity may be caused by two plastic effects present in the rise stage. The first effect is the reduction of the drop rising velocity with  $Pl$ . The second effect is the drop width reduction caused by the viscosity field of the Bingham material. Figure 19(a) and (b) exhibit the dimensionless viscosity field,  $\bar{\mu}_1$ , in the film (in the  $(s, h)$  coordinate system) and around the drop outside the film (in the  $(r, z)$  coordinate system), respectively, at the moment  $\bar{h}_{min} = 0.01$  for  $Pl = 0.04$ ,  $Fr = 200$ ,  $Bo = 2$ , and  $\mu_r = 10$ .

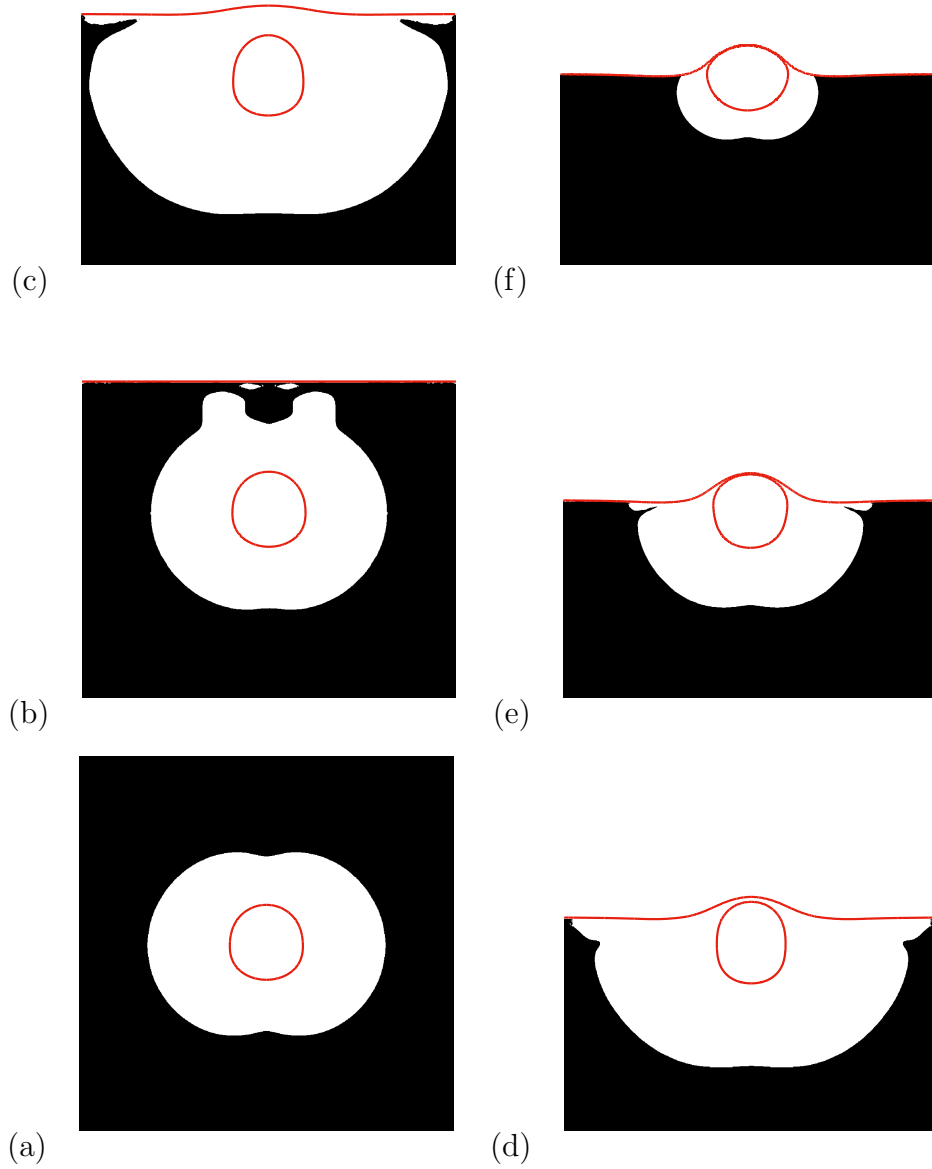


Figure 17: Yield surface around a drop rising and impacting on the top layer interface for  $Pl = 0.04$ ,  $Fr = 200$ ,  $Bo = 20$ ,  $\mu_r = 0.1$  at steady-state rise (a), approaching the interface at  $\bar{t}/(Fr^{1/2}) = -6.35$  (b) and  $-1.60$  (c), colliding on the interface at  $\bar{t}/(Fr^{1/2}) = 0.30$  (d) and  $1.25$  (e), and resting on the interface at  $\bar{t}/(Fr^{1/2}) = 2.75$  (f).

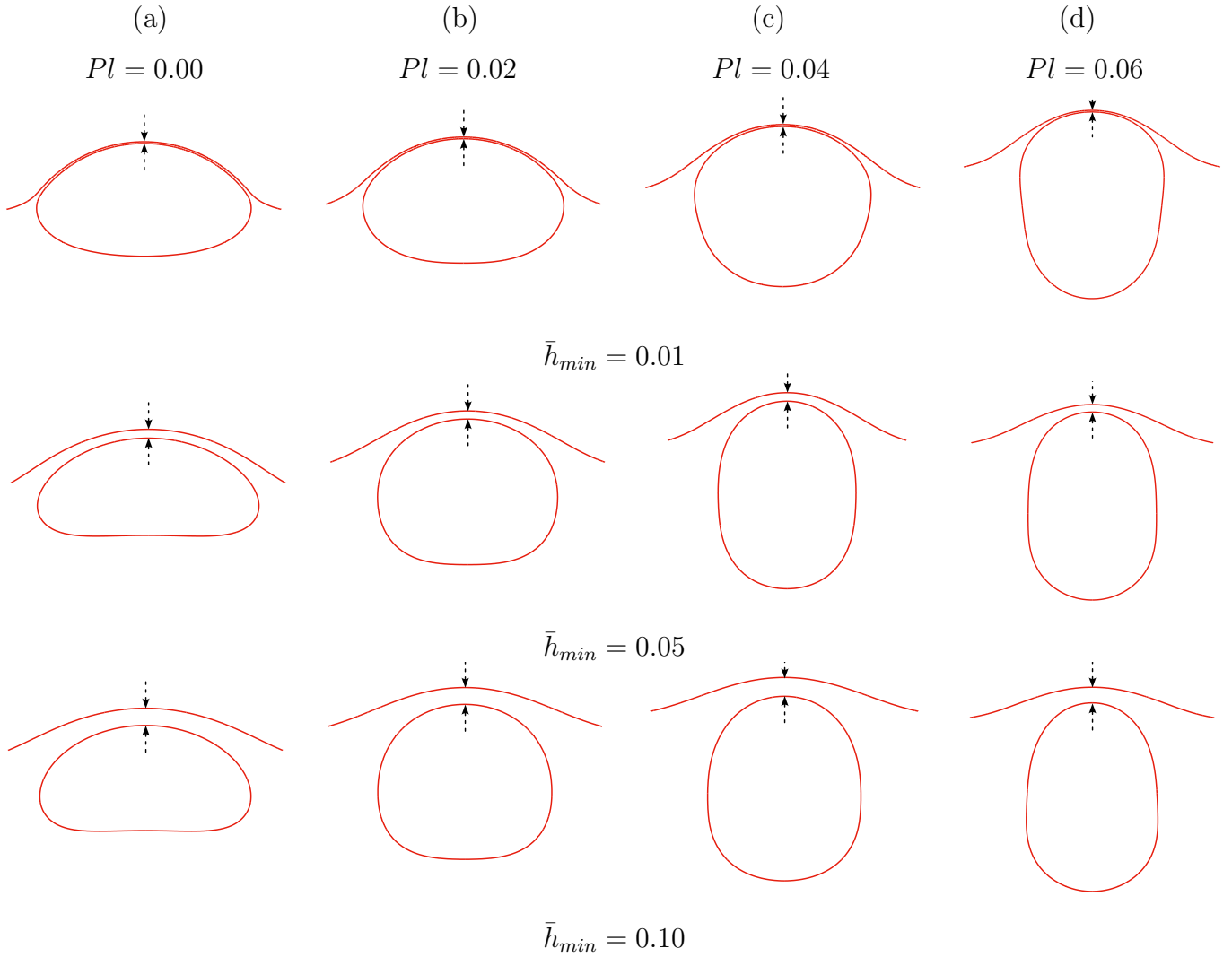


Figure 18: Drop and top layer interface shape for  $\bar{h}_{min} = 0.10$  (third row),  $\bar{h}_{min} = 0.05$  (second row), and  $\bar{h}_{min} = 0.01$  (first row) for  $Fr = 200$ ,  $Bo = 20$ ,  $\mu_r = 0.1$ , and (a)  $Pl = 0.00$ , (b)  $Pl = 0.02$ , (c)  $Pl = 0.04$ , and (d)  $Pl = 0.06$ . The film thinnest part is marked by a pair of black arrows.

As shown in Fig. 19(a), the viscosity in the film increases with  $\bar{s}$ . Hence, the film thins more quickly in the film center region than in the film periphery region. Moreover, Fig. 19(b) shows that the viscosity of the surrounding material close to the drop equator is higher than that close to the drop poles (as in the rise stage). Therefore, the drop width increase that eventually takes place during the collision stage seems to be hampered by plastic effects of the surrounding material. Sanjay et al. (2021) studied the merging of bubbles with a top layer gas in Bingham materials. They also observed a hampering of capillary waves and the shape change of the cavity formed after film rupture due to the yield stress of the surrounding. The impact of plasticity and surface tension on the interface deflection can be observed in Fig. 20, which illustrates the dimensionless position  $\bar{z}$  of the interface during the collision for various  $Pl$  and  $Bo$  values. The curves terminate at  $\bar{h}_{min} = 0.01$ . The outcomes signify that plasticity has a damping effect on drop collision, leading to a reduction in the amplitude and rate of interface deflection, irrespective of the Bond number value. Furthermore, a decrease in the Bond number also leads to a decrease in the maximum interface deformation due to the interface's lower deformability. Thus, our results suggest that an increase in plasticity and/or surface tension results in a decrease in drop rebound, which is observed only for  $Bo = 20$  and  $Pl = 0.00$  in Fig. 20.

Fig. 21(a) and (b) exhibit the dimensionless drop velocity (multiplied by  $Fr^{1/2}$ ),  $\bar{u}$ , and dimensionless width,  $\bar{D}_W$ , respectively, versus dimensionless time (divided by  $Fr^{1/2}$ ),  $\bar{t}$ , for  $Pl = 0.04$  and the same sets of  $Fr$ ,  $\mu_r$ , and  $Bo$  of Fig. 13 for  $Pl = 0.00$ . We take the purple line ( $Pl = 0.04$ ,

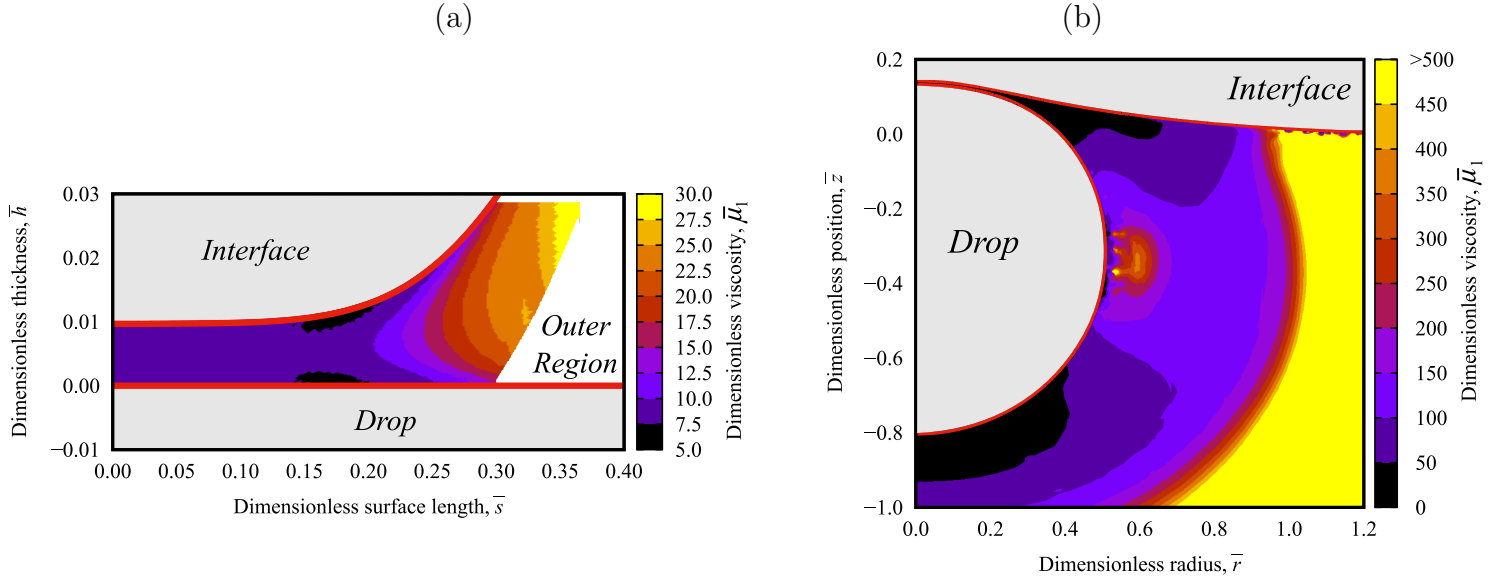


Figure 19: Dimensionless viscosity field (a) in the film in the  $(s, h)$  coordinate system and (b) around the drop in the  $(r, z)$  coordinate system at the moment  $\bar{h}_{min} = 0.01$  for  $Pl = 0.04$ ,  $Fr = 200$ ,  $Bo = 2$ , and  $\mu_r = 10$ . Gray areas correspond to Fluid 2 (drop and top layer).

$Fr = 200$ ,  $\mu_r = 0.1$ , and  $Bo = 2$ ) as the base scenario, and then change  $Fr$ ,  $\mu_r$ , and  $Bo$  one at a time. The black dashed line marks the time  $\bar{t} = 0.0$  at which  $\bar{h}_{min} = 0.1$ , and the colored dashed lines mark the time at which  $\bar{h}_{min} = 0.01$ . Additionally, Fig. 22 presents the film shape for  $\bar{h}_{min} = 0.01$  (except for  $Pl = 0.04$ , the other dimensionless parameters are the same as Fig. 15). The changes in  $\bar{u}$  and  $\bar{D}_W$  for different values of  $Fr$  (purple line for  $Fr = 200$  and yellow line for  $Fr = 2000$ ) are similar to those in the Newtonian case. The drop impact velocity and width increase with an increase in the Froude number. The purple and yellow lines in Fig. 22, for  $Fr = 200$  and  $2000$ , respectively, also depict that, as in the Newtonian case, the film length increases with the Froude number. Nevertheless, both films

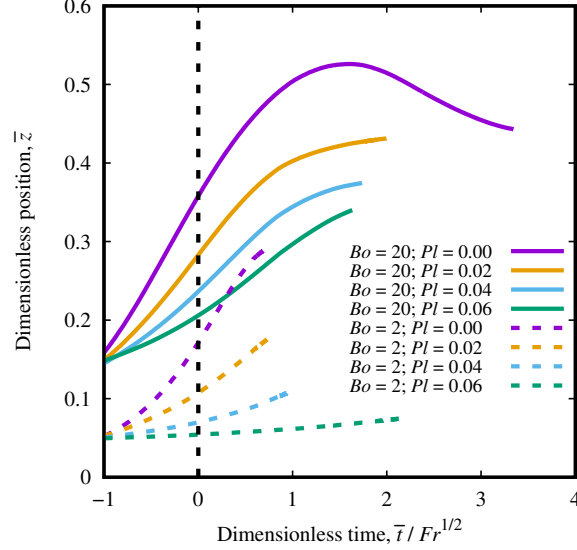


Figure 20: Interface dimensionless position,  $\bar{z}$ , with dimensionless time,  $\bar{t}$ , for  $Fr = 200$ ,  $\mu_r = 0.1$ ,  $Bo = 20$  (solid lines) and 2 (dashed lines), and  $Pl = 0.00$  (purple lines), 0.02 (yellow line), 0.04 (blue line), and 0.06 (green line).

have a spherical shape, while for the Newtonian case, the film for  $Fr = 2000$  forms a dimple. A similar behavior for an increase in the viscosity ratio as in the Newtonian case is also observed: the drop velocity and width change during the impact on the interface is smoother over a more extended period. Additionally, Deoclecio et al. (2021) have shown that the critical plastic number for drop entrapment reduces with an increase in  $\mu_r$ . Therefore, for the higher viscosity ratio (blue line in Fig. 21), the drop is closer to the entrapment condition than for the lower viscosity ratio. Hence, the velocity reduction with  $\mu_r$  is more significant than for the Newtonian scenario. The drop rise velocity is close to zero for  $Pl = 0.04$  and  $\mu_r = 10$ . The blue line in Fig. 22 for  $\mu_r = 10$  illustrates that the film remains spherical even for the

higher viscosity ratio case.

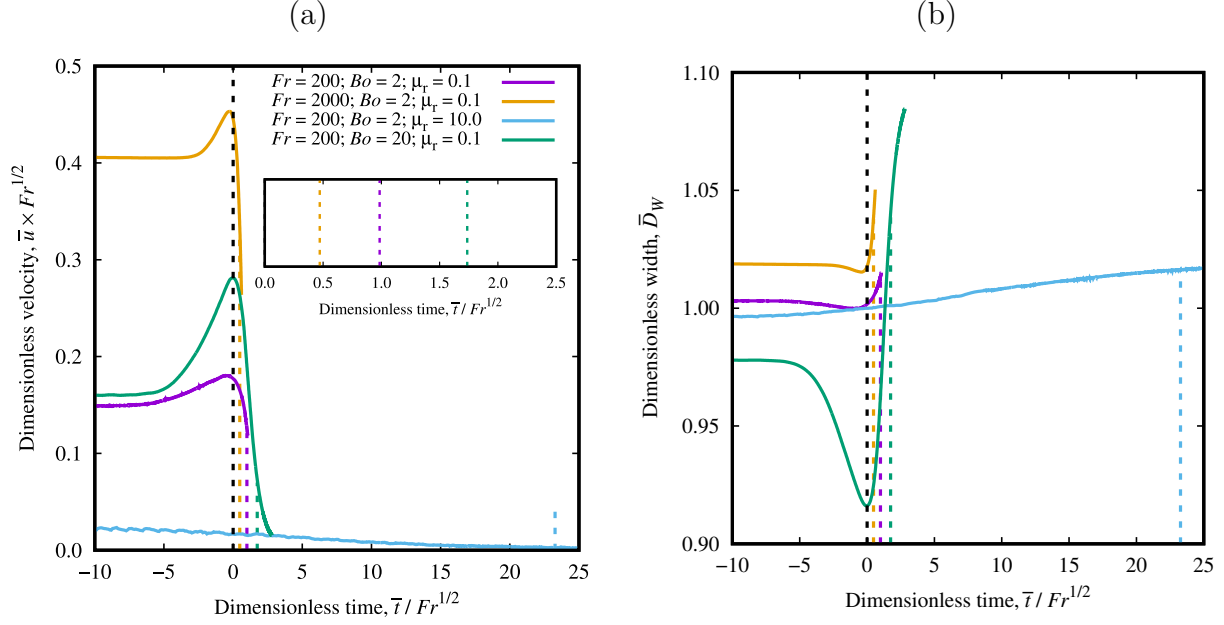


Figure 21: Drop (a) dimensionless velocity,  $\bar{u}$  ( $\times Fr^{1/2}$ ), and (b) dimensionless width,  $\bar{D}_{tW}$ , versus dimensionless time,  $\bar{t}$  ( $/Fr^{1/2}$ ). The dimensionless parameters are  $Pl = 0.04$ , (purple line)  $Fr = 200$ ,  $\mu_r = 0.1$ ,  $Bo = 2$ , (yellow line)  $Fr = 2000$ ,  $\mu_r = 0.1$ ,  $Bo = 2$ , (blue line)  $Fr = 200$ ,  $\mu_r = 10$ ,  $Bo = 2$ , and (green line)  $Fr = 200$ ,  $\mu_r = 0.1$ ,  $Bo = 20$ .

For an increase in the Bond number (purple and green lines for  $Bo = 2$  and 20, respectively, in Fig. 21), the drop rise and impact velocities ( $\bar{t} \lesssim 0.0$ ) increase, differently from the  $Pl = 0.00$  case. This effect is due to the drop width reduction with  $Pl$ , which is more pronounced for higher values of  $Bo$ . However, as the drop collision proceeds and kinetic energy is converted to surface energy, the drop width for  $Bo = 20$  becomes larger than for  $Bo = 2$ . As a result, the film length for  $Bo = 20$  eventually becomes more prominent

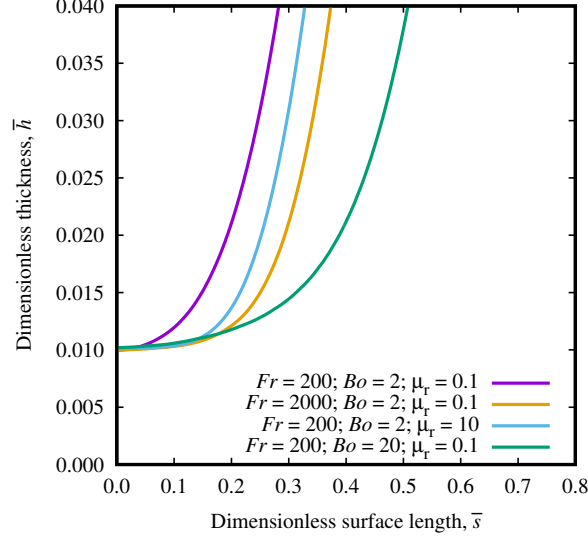


Figure 22: Film dimensionless thickness,  $\bar{h}$ , versus dimensionless surface length,  $\bar{s}$ , at  $\bar{h}_{min} = 0.01$ . The dimensionless parameters are  $Pl = 0.04$ , (purple line)  $Fr = 200$ ,  $\mu_r = 0.1$ ,  $Bo = 2$ , (yellow line)  $Fr = 2000$ ,  $\mu_r = 0.1$ ,  $Bo = 2$ , (blue line)  $Fr = 200$ ,  $\mu_r = 10$ ,  $Bo = 2$ , and (green line)  $Fr = 200$ ,  $\mu_r = 0.1$ ,  $Bo = 20$ .

than for  $Bo = 2$ , as shown by the green line in Fig. 22.

#### 4.3.2. The effect of $Pl$ on $\Delta\bar{t}$

In this section, we discuss the influence of plasticity on the initial stage of the film drainage process. The computational drainage time,  $\Delta t$ , is used to give a measure, or an indication, of how plasticity influences the coalescence time. Figure 23 presents the dimensionless computational drainage time (divided by  $Fr^{1/2}$ ),  $\Delta\bar{t}$ , as a function of  $Pl$  for the same sets of  $Fr$ ,  $\mu_r$ , and  $Bo$  of Fig. 10. In the base scenario (purple line for  $Fr = 200$ ,  $\mu_r = 0.1$ , and  $Bo = 2$ ), the computational drainage time increases with  $Pl$ . The same trend



is observed for the higher Froude number scenario (yellow line for  $Fr = 2000$ ) and the higher viscosity ratio scenario (blue line for  $\mu_r = 10$ ). The changes in  $\Delta\bar{t}$  with  $Fr$  and  $\mu_r$  are the same for all values of  $Pl$ . That is,  $\Delta\bar{t}$  decreases and increases with an increase in  $Fr$  and  $\mu_r$ , respectively. For the higher Bond number scenario (green line for  $Bo = 20$ ), an inverse trend is observed, and  $\Delta\bar{t}$  decreases with  $Pl$ .

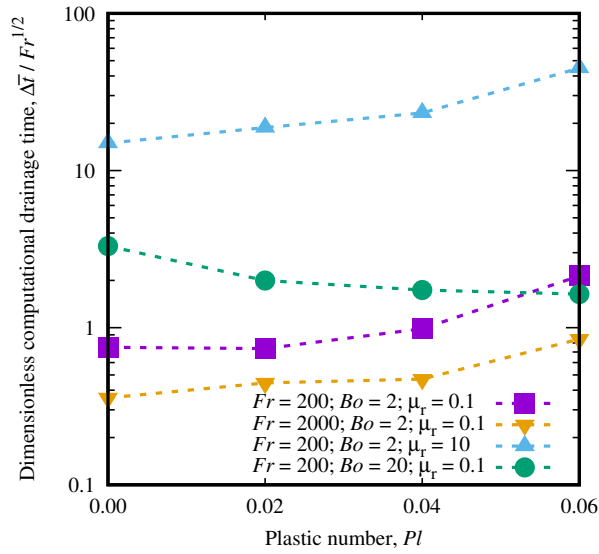


Figure 23: Dimensionless computational drainage time,  $\Delta\bar{t} (/Fr^{1/2})$ , versus the plastic number,  $Pl$ .

As discussed in the previous sections, the drainage time is a function of the film geometry (film length and shape) and the rheological properties of the phases (*e.g.*, interface mobility and viscous resistance). Plastic effects facilitate coalescence by forming prolate drops and spherical films on the one hand but make it more difficult by imposing a more excellent resistance to

the flow of the film on the other hand. To illustrate this, Fig. 24 shows the dimensionless stress field in the film for  $Fr = 200$ ,  $Bo = 2$ ,  $\mu_r = 10$ , and different values of  $Pl$  at  $\bar{h}_{min} = 0.01$ . Here, we try to elucidate how the film shape and how the magnitude (on average) of the stress in the film (which is linked to the rheological properties of the materials) change with  $Pl$ . It is worth noting that  $\bar{\tau}_y = Pl$ . The gray area corresponds to the Newtonian fluids of the drop and top layer interface, and the white area on the right to the region of the surrounding material outside the film. For  $Pl = 0.00$  (Fig. 24(a)), the film is dimpled, and a region of high stress is found on the film throat, while the stress in the film center region is small. This agrees with the theoretical results of Abid and Chesters (1994), who predicted that for dimpled films with partially mobile interfaces the maximum shear stress occurs close to the film rim. For  $Pl = 0.02$  (Fig. 24(b)), a similar trend is verified, but the film length and dimple size are smaller. The stress in the central region of the film is slightly above the yield stress ( $||\bar{\tau}|| \gtrsim \bar{\tau}_y$ ). For  $Pl = 0.04$  (Fig. 24(c)), the film length reduces, and it becomes spherical. Due to the shorter film, the buoyancy force is distributed over a smaller area, increasing the stress in the film, which is also slightly above the yield stress. A similar behavior is verified for  $Pl = 0.06$  (Fig. 24(d)). The film is even shorter, and the stress in the film is slightly above the yield stress. Therefore, increasing the plasticity of the surrounding materials makes the film more spherical and shorter, which facilitates drainage. This mechanism is more pronounced for higher values of the Bond number, which explains why  $\Delta\bar{t}$  decreases with  $Pl$  for  $Bo = 20$ . The minimum stress in the film is slightly above the yield stress in all cases, meaning that the strain rate

in the film is low ( $\|\bar{\tau}\| = \tau_y + \mu_p \|\dot{\gamma}\| \gtrsim \bar{\tau}_y$ , so  $\|\dot{\gamma}\| \approx 0.0$ ). Hence, the average viscosity in the film (*e.g.*,  $\mu_1 = \mu_p + \tau_y/\|\dot{\gamma}\|$ ) increases with  $Pl$ , making the drainage process more difficult. For lower values of  $Bo$ , surface tension is stronger, and the drop is less distorted by the distorting forces. In this case, the imposed flow resistance by the plasticity of the surrounding material overcomes the facilitation promoted by the film geometry and as a consequence,  $\Delta\bar{t}$  increases with  $Pl$ . Therefore, the flow-arresting property of the yield stress is counterbalanced by the film geometry change induced by it, which makes the determination of the arresting condition of the film challenging.

Goel and Ramachandran (2017) conducted a study on the drainage of Bingham materials films utilizing the lubrication theory and scaling analyses. The interfaces were immobile and the drops approached each other at a constant velocity (binary collision). The study focused on the drainage time as a function of the capillary number  $Ca = F/(\sigma R)$ , where  $F$  is the force pressing the drops together and  $R$  is the drops radius. While the interfaces' deformation and film thickness in our work are larger than those studied with the lubrication theory, and the constant force approach is more appropriate for interfacial coalescence than the constant velocity used by the authors, we attempt to make a qualitative comparison between their findings and our own. In the authors' study, the addition of a yield stress to the film materials was found to increase the drainage time for all capillary numbers. However, as pointed out by Thompson and Soares (2016), the yield stress has a dual nature, viscous and plastic. This can be seen in the definition of viscosity  $\mu = \|\tau\|/\|\dot{\gamma}\| = \tau_y/\|\dot{\gamma}\| + \mu_p$ , where an increase in  $\tau_y$  (keeping  $\mu_p$  constant)

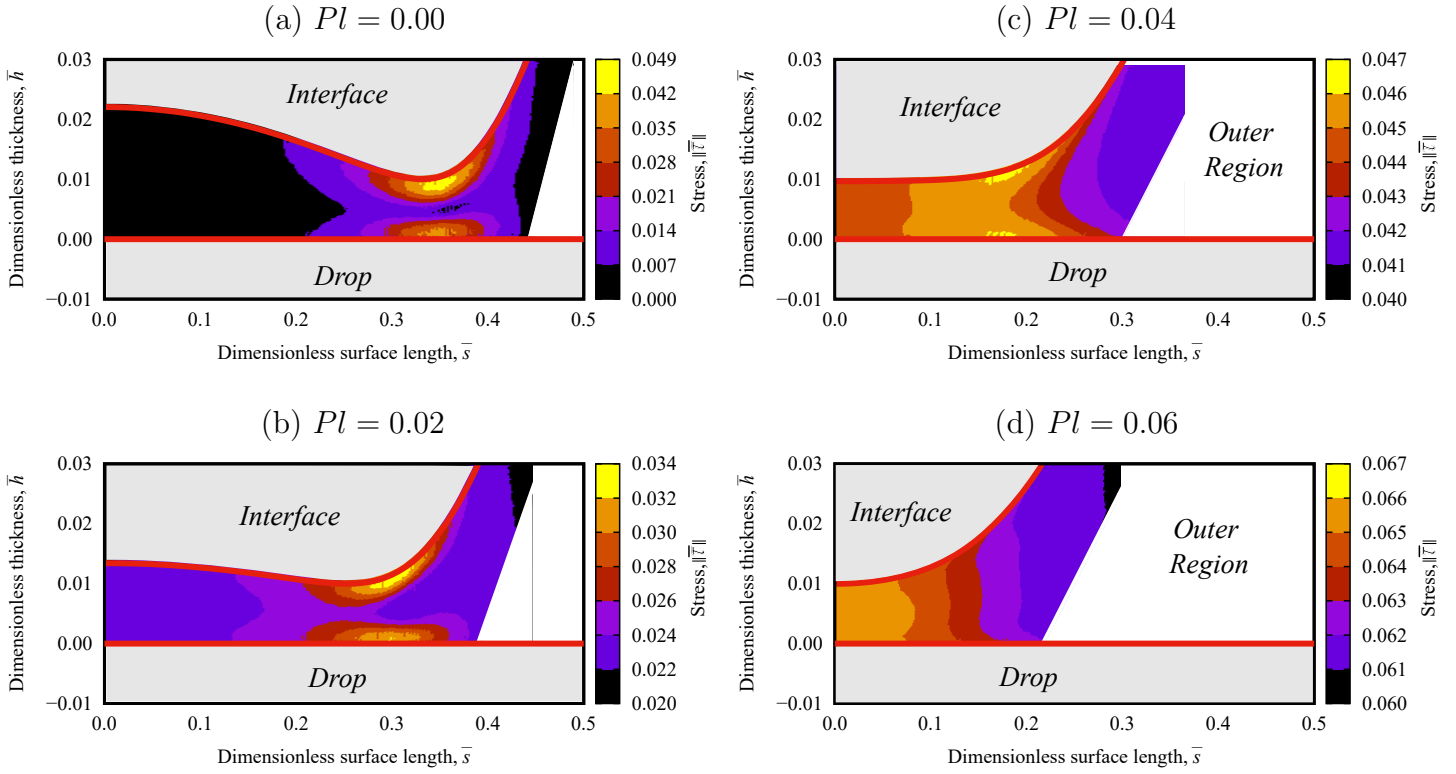


Figure 24: Dimensionless stress field  $\|\bar{\tau}\|$  at  $\bar{h}_{min} = 0.01$  for  $Fr = 200$ ,  $Bo = 2$ ,  $\mu_r = 10$ , and  $Pl = \bar{\tau}_y =$  (a) 0.00, (b) 0.02, (c) 0.04, and (d) 0.06. The gray areas correspond to Fluid 2 (Newtonian) and the white area corresponds to the region in Fluid 1 (viscoplastic) outside the film.

results in an increase in viscous resistive forces. Therefore, we argue that the increase in drainage time observed by the authors may be due to an increase in the viscosity of the surrounding, which has a similar impact of decreasing the Froude number in our study, and not necessarily of increasing the level of plasticity. In fact, we have shown that for low surface tension regimes, the drainage time may be reduced with an increase in  $Pl$  due to the formation of a shorter and spherical film. The authors scale the film length as  $\sqrt{hR}$  for spherical films. Therefore, for a constant force  $F$ , the pressure gradient in the film increases because the film length decreases during the drainage process. This caused the magnitude of the stress to increase as the film thickness decreased, making these films not susceptible to be frozen by the yield stress. In contrast, our simulations have revealed an opposite trend, as illustrated in Fig. 25, which displays the dimensionless stress field for  $Fr = 200$ ,  $Bo = 2$ ,  $\mu_r = 10$ , and  $Pl = 0.04$  at  $\bar{h}_{min} = 0.050$ ,  $0.025$ , and  $0.010$ . Our findings suggest that, on average, the stress level in a spherical film can decrease as the film thickness reduces. Therefore, our results imply that the drainage of spherical films may be vulnerable to being arrested by the yield stress as the drainage process progresses. Lastly, the authors argued that plastic effects may freeze only dimpled films since these films present a region of minor stress in the film center. However, considering the rise and collision dynamics, dimpled films are formed for low levels of plasticity, which may not be sufficient to arrest the drainage process. For higher levels of plasticity, the film is spherical and shorter, making the drainage process arresting by yield stress more difficult. Therefore, dimpled films observed for high value of  $\tau_y$  in their work may not be obtainable in our simulations.

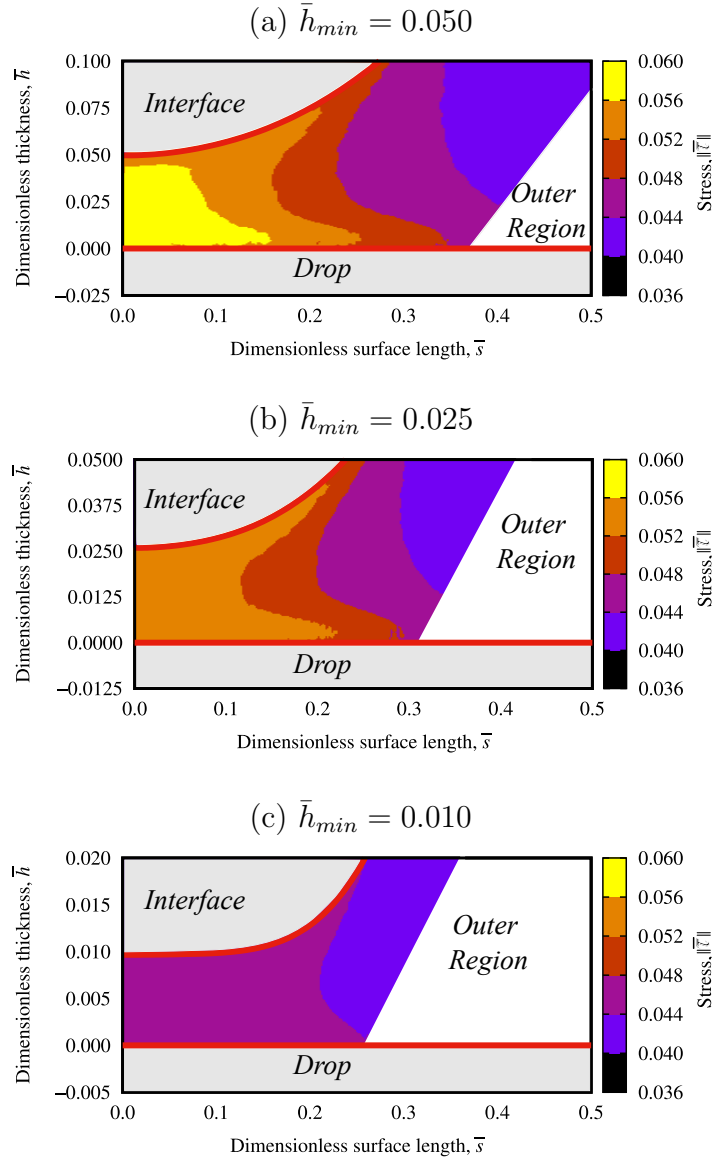


Figure 25: Dimensionless stress field  $\|\bar{\tau}\|$  for  $Fr = 200$ ,  $Bo = 2$ ,  $\mu_r = 10$ , and  $Pl = \bar{\tau}_y = 0.04$  at  $\bar{h}_{min} =$  (a) 0.050, (b) 0.025, and (c) 0.010. The gray areas correspond to Fluid 2 (Newtonian) and the white area corresponds to the region in Fluid 1 (viscoplastic) outside the film.

## 5. Concluding remarks

We have investigated the effects of the surrounding material plasticity on drop rise, collision with a liquid-liquid interface, and the initial stage of the film drainage process. The coalescence process, assessed based on the computational drainage time, depends on the film geometry (length and shape) and the rheological properties of the fluids. The decrease in viscous effects with an increase in the Froude number tends to overcompensate for the rise in inertial effects, which increase the film length and facilitate the formation of dimple-shaped films. As a result, the drainage time decreases with an increase in the Froude number. An increase in the viscosity ratio has the opposite effect. It enhances viscous dissipation and reduces inertial effects. In addition, the change in the film boundary condition with an increase in the viscosity ratio contributes to the formation of dimpled films. Consequently, an increase in the viscosity ratio tends to increase the drainage time. The drop deformation caused by plastic effects tends to facilitate the film drainage process by reducing the film length and forming spherical films. In contrast, the changes in the rheological parameters of the surrounding material tend to make the drainage process more difficult. The Bond number involves the shape-preserving surface tension force. An increase in  $Bo$  facilitates the deformation induced by the dominating distorting force, which enhances the influence of the film geometry on the beginning of the coalescence process. For small values of  $Bo$ , the interfaces are less distorted and the importance of the rheological properties of the phases, relative to the film geometry, on the coalescence time increases. For low values of  $Bo$ , an increase in the resistive force due to plasticity increases the drainage time with  $Pl$ . For high values of

*Bo*, the influence of the film geometry becomes more critical, and an increase in *Pl* facilitates the initial stage of the drainage process. The film arrest due to plastic effects depends on the balance between the film geometry and the level of plasticity of the surrounding material. Despite the low-stress region in dimple-shaped films, these were observed only for low levels of plasticity, in which the yield stress may not arrest the drainage process. An increase in the level of plasticity changes the film geometry in a way that hinders its arrest. Thus, the two opposing plastic effects make it difficult to determine the film's arresting condition.

## 6. Acknowledgment

This study was financed in part by the Coordenação de Aperfeiçoamento de Pessoal de Nível Superior - Brasil (CAPES) - Finance Code 001.

## References

- Aarts, D.G., Lekkerkerker, H.N., 2008. Droplet coalescence: drainage, film rupture and neck growth in ultralow interfacial tension systems. *Journal of fluid mechanics* 606, 275–294.
- Abid, S., Chesters, A., 1994. The drainage and rupture of partially-mobile films between colliding drops at constant approach velocity. *International journal of multiphase flow* 20, 613–629.
- Allouche, M., Frigaard, I.A., Sona, G., 2000. Static wall layers in the displacement of two visco-plastic fluids in a plane channel. *J. Fluid Mech.* 424, 243–277.



- Balla, M., Kavuri, S., Tripathi, M.K., Sahu, K.C., Govindarajan, R., 2020. Effect of viscosity and density ratios on two drops rising side by side. *Physical Review Fluids* 5, 013601.
- Balmforth, N.J., Frigaard, I.A., Ovarlez, G., 2014. Yielding to stress: recent developments in viscoplastic fluid mechanics. *Annual Review of Fluid Mechanics* 46, 121–146.
- Basilisk, . URL: <http://basilisk.fr/>.
- Beris, A., Tsamopoulos, J., Armstrong, R., Brown, R., 1985. Creeping motion of a sphere through a bingham plastic. *Journal of Fluid Mechanics* 158, 219–244.
- Bingham, E.C., 1922. *Fluidity and Plasticity*. McGraw-Hill, New York.
- Chan, D.Y., Klaseboer, E., Manica, R., 2011. Film drainage and coalescence between deformable drops and bubbles. *Soft Matter* 7, 2235–2264.
- Charin, A.H., Lage, P.L., Silva, L.F.L., Tuković, Ž., Jasak, H., 2019. On the dynamic behavior of rising droplets. *International Journal of Multiphase Flow* 110, 165–178.
- Chesters, A., 1991. Modelling of coalescence processes in fluid-liquid dispersions: a review of current understanding. *Chemical engineering research and design* 69, 259–270.
- Chhabra, R.P., 2006. *Bubbles, drops, and particles in non-Newtonian fluids*. CRC press.

- Chi, B., Leal, L., 1989. A theoretical study of the motion of a viscous drop toward a fluid interface at low reynolds number. *Journal of Fluid Mechanics* 201, 123–146.
- Chirco, L., Maarek, J., Popinet, S., Zaleski, S., 2022. Manifold death: a volume of fluid implementation of controlled topological changes in thin sheets by the signature method. *Journal of Computational Physics* 467, 111468.
- Clift, R., Grace, J.R., Weber, M.E., 2005. *Bubbles, drops, and particles* .
- Deka, H., Pierson, J.L., Soares, E.J., 2019. Retraction of a viscoplastic liquid sheet. *Journal of Non-Newtonian Fluid Mechanics* 272, 104172.
- Deka, H., Pierson, J.L., Soares, E.J., 2020. Retraction criteria of viscoplastic drops and sheets: Long-wave approximations. *Journal of Non-Newtonian Fluid Mechanics* 284, 104352.
- Deoclecio, L.H., Soares, E.J., Deka, H., Pierson, J.L., 2021. Bubble entrapment condition in bingham materials. *Journal of Non-Newtonian Fluid Mechanics* 295, 104616.
- Deoclecio, L.H.P., da Cunha Ribeiro, D., Meneguelo, A.P., 2020. Cfd modeling of the creaming zone of batch gravity separation with coalescence. *Journal of Dispersion Science and Technology* 41, 674–689. doi:10.1080/01932691.2019.1611436.
- Dimakopoulos, Y., Pavlidis, M., Tsamopoulos, J., 2013. Steady bubble rise in herschel–bulkley fluids and comparison of predictions via the augmented

- lagrangian method with those via the papanastasiou model. *Journal of Non-Newtonian Fluid Mechanics* 200, 34–51.
- Doubliez, L., 1991. The drainage and rupture of a non-foaming liquid film formed upon bubble impact with a free surface. *International journal of multiphase flow* 17, 783–803.
- Dubash, N., Frigaard, I., 2004. Conditions for static bubbles in viscoplastic fluids. *Physics of fluids* 16, 4319–4330.
- Dubash, N., Frigaard, I., 2007. Propagation and stopping of air bubbles in carbopol solutions. *Journal of non-newtonian fluid mechanics* 142, 123–134.
- Frigaard, I., Nouar, C., 2005. On the usage of viscosity regularisation methods for visco-plastic fluid flow computation. *Journal of non-newtonian fluid mechanics* 127, 1–26.
- Goel, S., Ramachandran, A., 2017. The suppression of droplet-droplet coalescence in a sheared yield stress fluid. *Journal of colloid and interface science* 492, 199–206.
- Hartland, S., Jeelani, A., 1987. Drainage in thin planar non-newtonian fluid films. *The Canadian Journal of Chemical Engineering* 65, 382–390.
- Hartland, S., Jeelani, S.A., 1986. Drainage of thin dimpled non-newtonian fluid films. *The Journal of Physical Chemistry* 90, 6054–6059.
- Henschke, M., Schlieper, L.H., Pfennig, A., 2002. Determination of a coales-

- cence parameter from batch-settling experiments. *Chemical Engineering Journal* 85, 369–378.
- Kamp, J., Villwock, J., Kraume, M., 2017. Drop coalescence in technical liquid/liquid applications: A review on experimental techniques and modeling approaches. *Reviews in Chemical Engineering* 33, 1–47.
- Kočárková, H., Rouyer, F., Pigeonneau, F., 2013. Film drainage of viscous liquid on top of bare bubble: Influence of the bond number. *Physics of Fluids* 25, 022105.
- Lagrée, P.Y., Staron, L., Popinet, S., 2011. The granular column collapse as a continuum: validity of a two-dimensional navier-stokes model with a  $\mu(i)$ -rheology. *Journal of Fluid Mechanics* 686, 378.
- Liao, Y., Lucas, D., 2010. A literature review on mechanisms and models for the coalescence process of fluid particles. *Chemical Engineering Science* 65, 2851–2864.
- Liu, B., Manica, R., Liu, Q., Klaseboer, E., Xu, Z., Xie, G., 2019. Coalescence of bubbles with mobile interfaces in water. *Physical review letters* 122, 194501.
- Mohamed-Kassim, Z., Longmire, E.K., 2003. Drop impact on a liquid–liquid interface. *Physics of Fluids* 15, 3263–3273.
- Oldenziel, G., Delfos, R., Westerweel, J., 2012. Measurements of liquid film thickness for a droplet at a two-fluid interface. *Physics of Fluids* 24, 022106.

- Popinet, S., 2009. An accurate adaptive solver for surface-tension-driven interfacial flows. *Journal of Computational Physics* 228, 5838–5866.
- Popinet, S., 2015. A quadtree-adaptive multigrid solver for the serre–green–naghdi equations. *Journal of Computational Physics* 302, 336–358.
- Sanjay, V., Lohse, D., Jalaal, M., 2021. Bursting bubble in a viscoplastic medium. *Journal of fluid mechanics* 922, A2.
- de Souza Mendes, P., 2011. Thixotropic elasto-viscoplastic model for structured fluids. *Soft Matter* 7, 2471–2483.
- Tchoukov, P., Yang, F., Xu, Z., Dabros, T., Czarnecki, J., Sjöblom, J., 2014. Role of asphaltenes in stabilizing thin liquid emulsion films. *Langmuir* 30, 3024–3033.
- Thompson, R.L., Soares, E..J., 2016. Viscoplastic dimensionless numbers. *Journal of Non-Newtonian Fluid Mechanics* 241, 60–69.
- Tripathi, M.K., Sahu, K.C., Karapetsas, G., Matar, O.K., 2015. Bubble rise dynamics in a viscoplastic material. *Journal of Non-Newtonian Fluid Mechanics* 222, 217–226.
- Tsamopoulos, J., Dimakopoulos, Y., Chatzidai, N., Karapetsas, G., Pavlidis, M., 2008. Steady bubble rise and deformation in newtonian and viscoplastic fluids and conditions for bubble entrapment. *Journal of Fluid Mechanics* 601, 123.
- Vakarelski, I.U., Langley, K.R., Yang, F., Thoroddsen, S.T., 2022. Interfer-

ometry and simulation of the thin liquid film between a free-rising bubble and a glass substrate. *Langmuir* 38, 2363–2371.

Vakarelski, I.U., Yang, F., Tian, Y.S., Li, E.Q., Chan, D.Y., Thoroddsen, S.T., 2019. Mobile-surface bubbles and droplets coalesce faster but bounce stronger. *Science advances* 5, eaaw4292.

Zawala, J., Malysa, K., 2011. Influence of the impact velocity and size of the film formed on bubble coalescence time at water surface. *Langmuir* 27, 2250–2257.

Zawala, J., Malysa, K., Kowalczyk, P.B., 2020. On importance of external conditions and properties of the interacting phases in formation and stability of symmetrical and unsymmetrical liquid films. *Advances in Colloid and Interface Science* 276, 102085.

Zenit, R., Magnaudet, J., 2008. Path instability of rising spheroidal air bubbles: a shape-controlled process. *Physics of Fluids* 20, 061702.